



1 **Development and Comparison of Empirical Models for All-sky Downward**
2 **Longwave Radiation Estimation at the Ocean Surface Using Long-term**
3 **Observations**

4 **Jianghai Peng^{1,2,3,4}, Bo Jiang^{1,2*}, Hui Liang^{1,2}, Shaopeng Li^{1,2}, Jiakun Han^{1,2}, Thomas C.**
5 **Ingalls^{3,4}, Jie Cheng^{1,2}, Yunjun Yao^{1,2}, Kun Jia^{1,2}, and Xiaotong Zhang^{1,2}**

6 ¹The State Key Laboratory of Remote Sensing Science, jointly sponsored by Beijing Normal University and
7 Institute of Remote Sensing and Digital Earth of Chinese Academy of Sciences, Beijing, China.

8 ²China and Beijing Engineering Research Center for Global Land Remote Sensing Products, Institute of
9 Remote Sensing Science and Engineering, Faculty of Geographical Science, Beijing Normal University,
10 Beijing, China.

11 ³Center for Global Discovery and Conservation Science, Arizona State University, Tempe, AZ, 85281, USA.

12 ⁴School of Earth and Space Exploration, Arizona State University, Tempe, AZ, 85281, USA.

13 Corresponding author: Bo Jiang(bojiang@bnu.edu.cn)

14



15 Abstract

16 The ocean-surface downward longwave radiation (R_1) is one of the most fundamental
17 components of the radiative energy balance, and it has a remarkable influence on air–sea
18 interactions. Because of various shortcomings and limits, a lot of empirical models were
19 established for ocean-surface R_1 estimation for practical applications. In this paper, based on
20 comprehensive measurements collected from 65 moored buoys distributed across global seas
21 from 1988 to 2019, a new model for estimating the all-sky ocean-surface R_1 at both hourly and
22 daily scales was built. The ocean-surface R_1 was formulated as a nonlinear function of the
23 screen-level air temperature, relative humidity, cloud fraction, total column cloud liquid, and ice
24 water. A comprehensive evaluation of this new model relative to eight existing models was
25 conducted under clear-sky and all-sky conditions at daytime/nighttime hourly and daily scales.
26 The validation results showed that the accuracy of the newly constructed model is superior to
27 other models, yielding overall RMSE values of 14.82 and 10.76 W/m² under clear-sky
28 conditions, and 15.95 and 10.27 W/m² under all-sky conditions, at hourly and daily scales,
29 respectively. Our analysis indicates that the effects of the total column cloud liquid and ice water
30 on the ocean-surface R_1 also need to be considered besides cloud cover. Overall, the newly
31 developed model has strong potential to be widely used.

32 *Keywords*: Ocean surface, longwave radiation, empirical model, buoy

33 1 Introduction

34 The downward longwave radiation (R_1) at the ocean surface is the thermal infrared (4–
35 100 μm) radiative flux emitted by the entire atmospheric column over the ocean surface (Yu et
36 al., 2018). The ocean-surface R_1 is among the most important components of the heat flux across
37 the ocean–atmosphere interface, which, in turn, shapes the climate state of both the atmosphere
38 and ocean (Caniaux, 2005; Fasullo et al., 2009; Fung et al., 1984). Therefore, an accurate
39 estimate of the ocean-surface R_1 is crucial for studies of air–sea interactions and the climate and
40 oceanic systems.

41 Although the ocean-surface R_1 is routinely measured at most buoy sites, the available
42 ocean-surface R_1 measurements can not meet the needs of various applications because of the
43 small number of buoys currently employed (especially moored buoys) and their sparse
44 distribution across global oceans. Another way to get the R_1 at the ocean surface is by using
45 satellite-based or model reanalysis products. The ocean-surface R_1 from satellite-derived
46 products, such as the International Satellite Cloud Climatology Project (ISCCP) (Rossow &
47 Zhang, 1995; Young et al., 2018) and Clouds and the Earth’s Radiant Energy System Synoptic
48 Radiative Fluxes and Clouds (CERES/SYN1deg) (Doelling et al., 2013; Rutan et al., 2015) is
49 usually generated using these satellite data and a radiative transfer model, which simulates the
50 radiative transfer interactions of light absorption, scattering, and emission through the
51 atmosphere with the input of given atmospheric parameters. However, radiative transfer models
52 are not widely used in practice because of their complicacy and the difficulties associated with
53 collecting all essential inputs. The ocean-surface R_1 provided in model reanalysis products, such
54 as the fifth generation of the European Centre for Medium-Range Weather Forecasts atmospheric
55 reanalysis of the global climate (ERA5) (Hersbach et al., 2020) and the Modern-Era
56 Retrospective analysis for Research and Applications, Version 2 (MERRA2) (Gelaro et al.,
57 2017), is produced by assimilating various observations into an atmospheric model to get the



58 optimal estimates of the state of the atmosphere and the surface (Gelaro et al., 2017). Previous
59 studies indicated that R_1 estimates from satellite-based products are generally in better agreement
60 with buoy measurements than those obtained from reanalysis products (Pinker et al., 2014;
61 Pinker et al., 2018; Thandlam & Rahaman, 2019). However, applications of the ocean-surface R_1
62 from these two kinds of products are limited due to their coarse spatial resolutions (most of them
63 are coarser than 1°), limited periods (especially satellite-based products), and discrepancies in
64 accuracy and consistency (Cronin et al., 2019). Hence, many parameterization and empirical
65 models for estimating ocean-surface R_1 that can easily be implemented in practical use have been
66 established during the past few decades (Bignami et al., 1995; Josey, 2003; Zapadka et al., 2001).
67 Most of the commonly used R_1 estimation models were established using the relationship
68 between R_1 and the relevant meteorological variables (i.e., air temperature, humidity, column
69 integrated water vapor (IWV), and cloud parameters) or oceanic parameters (i.e., bulk sea
70 surface temperature), which are usually obtained from in situ measurements or model
71 simulations (Li & Coimbra, 2019; Li et al., 2017; Paul, 2021). It is known that most R_1
72 estimation models were originally developed for the land surface and were applied to the ocean
73 surface directly without any alterations by assuming the atmospheric conditions are nearly the
74 same over ocean and land surfaces (Bignami et al., 1995; Clark et al., 1974; Frouin et al., 1988;
75 Josey, 2003). However, this assumption increases the uncertainty in R_1 estimates because of the
76 significantly different water vapor profiles over ocean and land surfaces (Bignami et al., 1995). A
77 few models built specifically for R_1 estimation at the ocean surface (Bignami et al., 1995; Josey,
78 2003; Zapadka et al., 2001) were usually developed using limited observations collected from
79 buoy sites or cruise ships distributed within a specific region; hence, the robustness of these
80 models were in doubt when applied globally. For example, Josey (2003) proposed a model for R_1
81 estimation at mid-high latitude seas with a satisfactory validation accuracy, but this new model
82 performed worse over tropical seas with a tendency to underestimate R_1 by up to $10\text{--}15\text{ W/m}^2$.
83 Moreover, most of the existing R_1 estimation models only work under clear-sky conditions,
84 which are especially rare over ocean surfaces. Furthermore, most of these models only derive R_1
85 at instantaneous scales, yet the R_1 at the daily scale is more preferred across a range of
86 applications. Therefore, a new, easily implemented model that can derive accurate and robust R_1
87 estimates at the global ocean surface under all-sky conditions at various temporal scales (e.g.,
88 instantaneous and daily) is required. More details about the existing R_1 estimation models are
89 given in Section 2.

90 In addition, according to W Wang and Liang (2009b), the uncertainty of the ocean-surface
91 R_1 estimation should be less than 10 W/m^2 for climate diagnostic studies. However, the
92 performances of the most commonly used R_1 estimation models at the global ocean surface were
93 not thoroughly evaluated in previous studies because of the few available in situ measurements.
94 Fortunately, being aware of the significance of the energy budget in air–sea interactions
95 (Centurioni et al., 2019), more and more platforms for radiative measuring have been built across
96 global ocean surfaces during the past decades, so relatively comprehensive ocean-surface R_1
97 measurements can be collected today, which provide a good opportunity for modeling and
98 comprehensive evaluations.

99 Overall, the main goal of this research is to establish a new empirical model for
100 calculating the all-sky ocean-surface R_1 at instantaneous and daily scales based on globally
101 distributed moored buoy measurements and other ancillary information. A comprehensive
102 evaluation is conducted on the newly developed model relative to eight commonly used models
103 for ocean-surface R_1 estimation under clear- and all-sky conditions at hourly and daily scales.



104 The organization of this paper is as follows. A review of the eight commonly used R_1 estimation
 105 models is presented in Section 2. Section 3 introduces the data sets used in this research and the
 106 methods, including the new model development and model evaluation. Section 4 shows the
 107 results of the model validation, comparison, and analysis. The key conclusions and discussions
 108 are provided in Section 5.

109 2 Review of Previous Models

110 Many models were proposed for R_1 calculation under various sky conditions at different
 111 temporal scales in previous studies. In this study, eight widely used models were selected for
 112 evaluation and Table 1 shows their basic information. According to the sky conditions under
 113 which these models could be used, the eight R_1 estimation models were divided into two classes:
 114 R_1 models under clear-sky conditions and under all-sky conditions, respectively. Details of the
 115 eight models are provided one by one in the following section. Note that the downward direction
 116 is defined as positive in this study.

117 **Table 1**
 118 *Eight Existing Models for Ocean-surface R_1 Estimation*

Sky Condition	Model	Abbr	Designed temporal scale	Reference
Clear-sky	$R_1 = a\sigma T_a^4(1+b\sqrt{e})$	Mod1	Monthly	Brunt (1932)
	$R_1 = \sigma T_a^4 \{1 - a \exp(-b(273 - T_a)^2)\}$	Mod2	5–15 minute	Idso and Jackson (1969)
	$R_1 = a\sigma T_a^4 (e/T_a)^{1/7}$	Mod3	Instantaneous	Brutsaert (1975)
	$R_1 = a\sigma T_a^4 [1 - \exp(-e^{T_a/2016})]$	Mod4	Daily	Satterlund (1979)
	$R_1 = \sigma T_a^4 [1 - (1 + \epsilon) \exp\{-(1.2 + 3\epsilon)^{1/2}\}]$ $\epsilon = 46.5 \left(\frac{e}{T_a}\right)$	Mod5	Instantaneous	Prata (1996)
All-sky	$R_1 = \frac{\epsilon\sigma T_s^4 - \epsilon\sigma T_s^4(a+b\sqrt{e})(1-\lambda C^2) + 4\epsilon\sigma T_s^3(T_s - T_a)}{1 - \alpha_1}$	Mod6	Daily	Clark et al. (1974)
	$R_1 = \sigma T_a^4(a+be)(1+dC^2)$	Mod7	Hourly	Bignami et al. (1995)
	$R_1 = \sigma \{T_a + aC^2 + bC - d + g(D+f)\}^4$	Mod8	Hourly	Josey (2003)

119 2.1 Under clear-sky condition

120 Among the eight models, there are five R_1 estimation models that could only be used
 121 under clear-sky conditions.

122 Brunt (1932) developed the first R_1 estimation model (named Mod1) for land surfaces,
 123 which relates the monthly mean R_1 to the screen-level water vapor and air temperature, as
 124 Equation (1) shows:

$$125 R_1 = a_1 \sigma T_a^4 (1 + b_1 \sqrt{e}) \quad (1)$$

126 where a_1 and b_1 are empirical coefficients, T_a is the monthly mean screen-level air



127 temperature (K), e is the monthly mean screen-level water vapor pressure (mbar), and σ is the
128 Stefan–Boltzmann constant, defined as $5.67 \times 10^{-8} \text{ W}/(\text{m}^2 \cdot \text{K}^4)$. In the study of Brunt (1932), the
129 two coefficients a_1 and b_1 were suggested as 0.52 and 0.125 based on observations collected from
130 Benson, South Oxfordshire, England. The validation results of Mod1 showed a correlation
131 coefficient as high as 0.97 based on the collected samples. However, Swinbank (1963) pointed
132 out that the validation results of Mod1 for other regions where variations in the humidity and T_a
133 were different from those in Benson were worse. Despite these limitations, as the first empirical
134 R_1 estimation model in a simple format, Mod1 has been widely used to construct the coupling
135 between hydrological and atmospheric models (Habets et al., 1999; Lohmann et al., 1998).

136 Different from Mod1, the model developed by Idso and Jackson (1969) (named Mod2)
137 was based on the theoretical consideration that the effective emittance of an atmosphere is solely
138 temperature-dependent; hence, the screen-level T_a is the only input of Mod2 for calculating R_1 :

$$139 \quad R_1 = \sigma T_a^4 \{1 - a_2 \exp(-b_2(273 - T_a)^2)\} \quad (2)$$

140 where a_2 and b_2 are empirical coefficients, which were defined as 0.261 and 7.770×10^{-4} ,
141 respectively, by Idso and Jackson (1969) based on experimental data at four sites located in
142 Arizona, Alaska, Australia, and the Indian Ocean, obtained at intervals of 5 to 15 minutes. Idso
143 and Jackson (1969) thought that Mod2 might be efficient at all latitudes for different seasons, as
144 it has been developed by using observations from diverse locations. Since publication, Mod2 has
145 been employed in relevant researches like evaporation estimation (Cleugh et al., 2007; Vertessy
146 et al., 1993) and ocean-ice modeling (Saucier et al., 2003).

147 Afterwards, Brutsaert (1975) proposed a simple model for computing R_1 by directly
148 solving the Schwarzschild's transfer equation (Schwarzschild, 1914) under clear skies and
149 standard atmospheric conditions (i.e., the U.S. 1962 standard atmosphere). This model is denoted
150 as Mod3, and is described as follows:

$$151 \quad R_1 = a_3 \sigma T_a^4 (e/T_a)^{1/7} \quad (3)$$

152 where a_3 is defined as a constant equal to 1.24, as determined during the Schwarzschild's
153 transfer equation solving process. Explicit physical theory is reflected in Mod3. The term
154 $(e/T_a)^{1/7}$, regarded as the atmospheric emissivity, tends to zero when the water vapor content is
155 very little. However, Prata (1996) indicated that the atmospheric emissivity tends to a certain
156 constant value even without water vapor, such as values from 0.17 to 0.19 when only CO_2 is
157 present (Staley & Jurica, 1972). The estimates from Mod3 are usually used as the necessary
158 inputs of hydrological models (Pauwels et al., 2007; Rigon et al., 2006) and climate models
159 (Mills, 1997).

160 Aase and Idso (1978) found that Mod2 and Mod3 performed poor when T_a was below
161 freezing. To address this issue, Satterlund (1979) proposed a model (named Mod4) to compute R_1
162 by reformatting T_a and e , as follows:

$$163 \quad R_1 = a_4 \sigma T_a^4 [1 - \exp(-e^{T_a/2016})] \quad (4)$$

164 where a_4 is an empirical coefficient and defined as 1.08 by Satterlund (1979) based on
165 collected daily R_1 measurements at one site in Sidney, Montana, USA. After validation and
166 comparison, Satterlund (1979) concluded that Mod4 outperformed Mod2 and Mod3 under
167 extreme conditions in terms of temperature and humidity and performed comparably with the
168 two models for other cases. As such, the R_1 estimates from Mod4 have been used in studies such



169 as snow pack evolution (Douville et al., 1995) and hydrological models (Schlosser et al., 1997).
170 However, because the model does not contain a constant term, the application of Mod4 should be
171 done with caution if the surface water vapor pressure is very close to zero.

172 With the development of radiation measuring instruments and technology, several new R_1
173 estimation models have been proposed, such as the model proposed by Prata (1996) (named
174 Mod5), as follows:

$$175 \quad R_1 = \sigma T_a^4 \left[1 - \left(1 + 46.5 \left(\frac{e}{T_a} \right) \right) \exp \left\{ - \left(a_5 + 46.5 b_5 \left(\frac{e}{T_a} \right) \right)^{1/2} \right\} \right] \quad (5)$$

176 where a_5 and b_5 are empirical coefficients, defined as 1.2 and 3.0 in the study of Prata
177 (1996) and Robinson (1947; 1950). As with Mod1–Mod4, Mod5 is also dependent on T_a and e
178 but contains a majorly revised right term (in the square brackets), which is regarded as the
179 emissivity. After extensive validation and comparison, Prata (1996) claimed Mod5 outperformed
180 or performed similar to other R_1 estimation models, including Mod1–Mod4, in areas within the
181 polar region, mid-latitudes, and tropical regions. Hence, Mod5 has been applied widely, from
182 studies of snowmelt modeling (Jost et al., 2009) to urban energy budget (Nice et al., 2018;
183 Oleson et al., 2008).

184 To sum up, all five R_1 estimation models (Mod1–Mod5) that only work under clear-sky
185 conditions take T_a and/or e as inputs. Such an approach is in agreement with the research of
186 Kjaersgaard et al. (2007) who found that R_1 is mainly emanated from the low-level atmosphere
187 that can be adequately characterized in terms of T_a and humidity under clear-sky conditions
188 (Diak et al., 2000; Ellingson, 1995; Prata, 1996). Moreover, the five models were all established
189 by using measurements from different regions at various timescales, and they can be employed at
190 any timescale (see Table 1) regardless of the temporal resolution of the original measurements
191 used for modeling.

192 2.2 Under all-sky condition

193 Three R_1 estimation models that can work under all-sky conditions were evaluated in this
194 paper. Comparing to the above five models, ancillary information (e.g., clouds) should be taken
195 into account in addition to T_a and e in the three models, and the three models were developed
196 specifically for ocean surfaces.

197 Based on the model developed by Clark et al. (1974) for the all-sky net longwave
198 radiation at the ocean surface (R_{1net} , the difference between the downward and upward longwave
199 radiation) calculation, Josey (2003) proposed a revised model (named Mod6) to estimate the all-
200 sky ocean-surface R_1 by getting rid of the ocean-surface upward longwave radiation as:

$$201 \quad R_1 = \frac{\varepsilon_s \sigma SST^4 - \varepsilon_s \sigma SST^4 (a_6 + b_6 \sqrt{e}) (1 - \lambda C^2) - 4 \varepsilon_s \sigma SST^3 (SST - T_a)}{1 - \alpha_s} \quad (6)$$

202 where ε_s is the sea surface emissivity, defined as a constant value of 0.98, and SST is the
203 sea surface temperature (K); hence, the term $\varepsilon_s \sigma SST^4$ is the upward longwave radiation at the
204 ocean surface. α_s is the sea surface longwave radiation reflectivity, defined as a constant value of
205 0.045, C is the cloud cover (0–1; dimensionless), λ is a latitude-dependent coefficient that
206 represents the cloud amount, and a_6 and b_6 are empirical coefficients. Based on measurements
207 (i.e., R_1 , T_s , and C) collected from the Chemical and Hydrographic Atlantic Ocean Section
208 (CHAOS) in the northeast Atlantic in 1998, a_6 and b_6 were determined as 0.39 and -0.05 (Clark et



209 al., 1974; Josey, 2003), and λ at a given latitude can be taken from Josey et al. (1997). Josey
210 (2003) validated Mod6 and the results showed that Mod6 tended to overestimate the
211 instantaneous R_1 measurements from CHAOS by 11.70 W/m^2 . The estimates from Mod6 have
212 been applied in hydrodynamic models (Grayek et al., 2011) and atmospheric boundary layer
213 models (Deremble et al., 2013).

214 Based on hourly cruise measurements (i.e., R_1 , T_a , and C) collected in the Mediterranean
215 Sea during the period from 1989 to 1992, Bignami et al. (1995) proposed an empirical model to
216 calculate the ocean-surface all-sky R_1 (named Mod7) as follows:

$$217 \quad R_1 = \sigma T_a^4 (a_7 + b_7 e) (1 + c_7 C^2) \quad (7)$$

218 where a_7 , b_7 , and c_7 are empirical coefficients defined as 0.684, 0.0056, and 0.1762,
219 respectively. Bignami et al. (1995) presented validated RMSE values for Mod7 which ranged
220 from $\sim 14 \text{ W/m}^2$ at the hourly scale to $\sim 9 \text{ W/m}^2$ at the daily scale. Mod7 has been utilized by the
221 Mediterranean Forecasting System for predictions of currents and biochemical parameters
222 (Pinardi et al., 2003), coupled ocean–atmosphere climate models (Dubois et al., 2012) as well as
223 generation of the Atlantic Ocean heat flux climatology (Lindau, 2012).

224 Also based on the measurements collected from CHAOS, Josey (2003) assessed the
225 accuracy of Mod7 and found that this model tended to underestimate the all-sky R_1 by 12.10
226 W/m^2 at the instantaneous scale. After analyzing the shortcomings of Mod6 and Mod7, Josey
227 (2003) proposed a new model (named Mod8) for all-sky ocean-surface R_1 calculation through a
228 revision of T_a by using the same samples:

$$229 \quad R_1 = \sigma \{ T_a + a_8 C^2 + b_8 C - c_8 + d_1 (D + e_1) \}^4 \quad (8)$$

230 where a_8 , b_8 , c_8 , d_1 , and e_1 are empirical coefficients determined as 10.77, 2.34, 18.44,
231 0.84, and 4.01, respectively, D is the dew point depression, and T_a is the temperature (K) (see
232 Equation (11)). Estimates of R_1 obtained with Mod8 agreed to within 2 W/m^2 in the mean bias of
233 10 minute measurements at middle-high latitudes. The estimates from Mod8 have been used as
234 essential input in simulations of ocean–atmosphere interactions in the Arctic shelf (Cottier et al.,
235 2007).

236 Overall, it was thought that variations in the all-sky ocean-surface R_1 were related to T_a , e ,
237 and cloud information (e.g., cloud cover and cloud amount) in previous studies. However, Fung
238 et al. (1984) pointed out that other relevant cloud information, such as the cloud base height
239 (CBH) and cloud optical thickness, also have a significant influence on ocean-surface longwave
240 radiation. Therefore, more efforts should be made to increase the R_1 estimation accuracy under
241 all-sky conditions.

242 **3 Data and Methodology**

243 In order to develop a new all-sky ocean-surface R_1 estimation model, the meteorological
244 and radiative observations from 65 moored buoys and the cloud parameters from the ERA5
245 reanalysis product from 1988 to 2019 were applied. Afterwards, the newly developed model and
246 the eight commonly used models (Mod1–Mod8) were evaluated against the moored R_1
247 measurements under clear- and all-sky conditions at hourly/daily scales



248 3.1 Data and pre-processing

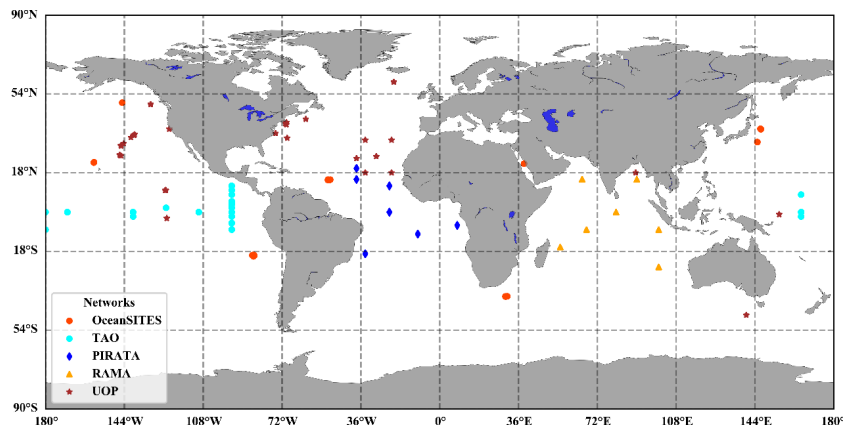
249 Table 2 lists all the variables employed in this paper and their information. The
 250 instantaneous timescale can be defined as timescales ranging from a 3 minute average to hourly
 251 average (Bignami et al. (1995); K Wang and Liang (2009a); hence, two timescales, hourly and
 252 daily, were considered in this study for model evaluation as in previous studies (Bilbao & de
 253 Miguel, 2007; Kjaersgaard et al., 2007; Sridhar & Elliott, 2002). Note that Mod1 was also used
 254 at the two timescales (Guo et al., 2019) though it was originally established with monthly
 255 samples. More details about the data are given below.

256 **Table 2**
 257 *Variables: Explanations and Sources*

Abbreviation	Full name	Time scales	Unit	Source
RH	Relative humidity	Daily/hourly	%	In situ
e	Water vapor	Daily/hourly	hPa	Calculated
T _a	2-m air temperature	Daily/hourly	K	In situ
T _s	Sea surface temperature	Daily/hourly	K	In situ
D	Dew point depression	Daily/hourly	K	Calculated
CI	Clearness index	Daily/hourly	0-1	Calculated
C	Fractional cloud cover	Daily/hourly	0-1	Calculated
clw	Total column cloud liquid water	Daily/hourly	g/m ²	ERA5
ciw	Total column cloud ice water	Daily/hourly	g/m ²	ERA5

258 3.1.1 Measurements from moored buoys

259 All measurements were collected from 65 moored buoy sites, whose latitudes range from
 260 47°S to 59.5°N, as shown in Figure 1. The majority of moored buoy sites were located in
 261 tropical seas (23.5°S–23.5°N), and relatively few buoys were in the high-latitude seas of the
 262 Northern Hemisphere (>50°N) and the mid-high latitude seas of the Southern Hemisphere
 263 (>30°S).



264
 265 **Figure 1.** Spatial distribution of the 65 moored buoys.

266 The moored buoy sites in this study belong to five well-known observation
 267 network/programs, including the Upper Ocean Processes Group (UOP), Tropical Atmosphere
 268 Ocean/Triangle Trans-Ocean Buoy Network (TAO/TRITON), Pilot Research Moored Array in



269 the Tropical Atlantic (PIRATA), Research Moored Array for African–Asian–Australian Monsoon
 270 Analysis and Prediction (RAMA), and OceanSITES. Launched by the Woods Hole
 271 Oceanographic Institution (WHOI), UOP mainly focuses on studying the physical processes of
 272 the air-sea interface and the epipelagic, and its buoys are equipped with oceanographic and
 273 meteorological sensors. The UOP measurements accurately quantify annual cycles of wind stress
 274 and net air-sea heat exchange in the Southern Ocean (Schulz et al., 2012). Twenty-two sites form
 275 the UOP, and data from all were used in this study. TAO/TRITON (McPhaden et al., 1998) in the
 276 tropical Pacific, PIRATA (Bourlès et al., 2008) in the tropical Atlantic, and RAMA in the tropical
 277 Indian Ocean (McPhaden et al., 2009) are all part of the Global Tropical Moored Buoy Array
 278 (GTMBA) program (McPhaden et al., 2010). Extensive quality control was done by GTMBA
 279 prior to dissemination of the data (Freitag, 1999; 2001; Lake, 2003; Medovaya et al., 2002), and
 280 they have been used for monitoring, understanding, and forecasting the El Niño–Southern
 281 Oscillation (ENSO) and monsoon variability (McPhaden et al., 2009). Data from 35 GTMBA
 282 sites (TAO, 21; PIRATA, 7; RAMA, 7) were used in this study. The OceanSITES network is
 283 composed of buoys funded by oceanographic researchers across the globe. The goal of the
 284 OceanSITES program is to facilitate the use of high-quality multidisciplinary data from fixed
 285 sites in the open ocean (Cronin et al., 2019). Eight sites from OceanSITES were utilized. In this
 286 study, the routine measurements made at moored buoys, including radiative measurements (e.g.,
 287 ocean-surface downward shortwave radiation R_g) and meteorological measurements (e.g., T_a and
 288 RH) were collected and used; other variables (e.g., e , D , and CI) were calculated from these
 289 measurements. More information regarding these data sets is found in Table 3.

290 **Table 3**
 291 *Descriptions of Different Networks*

Network/Program	No. of sites	Period	Observation frequency	Variables	URL
UOP	22	1988-2017	1 hour	R_i , R_g , T_a , RH	http://uop.who.edu/index.html
TAO/TRITON	21	2000-2019	10 min	R_i , R_g , T_a , RH	https://www.pmel.noaa.gov/tao/drupal/disdel/
RAMA	7	2004-2019	10 min	R_i , R_g , T_a , RH	https://www.pmel.noaa.gov/tao/drupal/disdel/
PIRATA	7	2006-2019	10 min	R_i , R_g , T_a , RH	https://www.pmel.noaa.gov/tao/drupal/disdel/
OceanSITES	8	2000-2018	1 hour	R_i , R_g , T_a , RH	http://www.oceansites.org/

292 3.1.1.1 Radiative measurements

293 At each moored buoy, R_i is routinely measured by an Eppley Precision Infrared
 294 Radiometer (PIR) with a nominal accuracy of $\pm 1\%$ (Richard E. Payne & Anderson, 1999), and
 295 R_g is routinely measured by an Eppley Laboratory precision spectral pyranometer (PSP) with a
 296 calibration accuracy of $\pm 2\%$ (Freitag, 1994). The PIR and PSP are deployed approximately 3 m
 297 above sea level. All measurements are quality controlled by their providers. To ensure data
 298 quality, a two step approach was implemented; 1) only observations flagged as ‘high quality’ by
 299 the data providers were considered, and 2) data was manually inspected by the authors for any
 300 irregularities. Additionally, the R_i measurements above 450 W/m^2 were removed, as suggested
 301 by Josey (2003).

302 As pointed out by Pascal and Josey (2000), the main errors in measuring R_i are from the



303 shortwave leakage and differential heating of the sensor. Therefore, the errors (ΔR_1) in R_1
304 observations were corrected according to Pascal and Josey (2000) as:

$$305 \quad \Delta R_1 = (a + \lambda)R_g + bR_g^2 \quad (9)$$

306 where $a = 4.34 \times 10^{-3}$, $\lambda = 0.011$, and $b = 1.72 \times 10^{-6}$. Hence, the R_1 measurements at a
307 sampling frequency less than one hour were first corrected. After that, selected measurements
308 whose sampling frequency was less than one hour were aggregated into hourly means as long as
309 80% of the measurements in one hour were available, and the hourly data were aggregated into
310 daily means as long as 24 hourly data in one day were available.

311 Note that the errors of the measured R_g induced by buoy rocking motions, sensor tilting,
312 and aerosol accumulation (Medovaya et al., 2002) were too small to be considered here. At last,
313 47,266 samples at the daily scale and 1,275,308 samples at the hourly scale during the period
314 from 1988 to 2019 were used in this study. For better comparison, the hourly samples used for
315 independent validation were further divided into daytime ($R_g > 120 \text{ W/m}^2$) and nighttime
316 conditions ($R_g \leq 120 \text{ W/m}^2$), with 147,981 samples in daytime and 210,057 in nighttime.

317 3.1.1.2 Meteorological and oceanic variables

318 Two meteorological measurements, RH and T_a , were collected at the moored buoy sites.
319 The instrument used for measuring RH and T_a is a Rotronic MP-100F, deployed about 3 m above
320 the sea level. The instrument produced accuracies of 2.7% and 0.2 K (Lake, 2003) for RH and
321 T_a , respectively, which are also too small to influence the accuracy of the R_1 estimation. Similar
322 to the radiative measurements, RH and T_a were both strictly screened and then aggregated into
323 hourly and daily means.

324 On the contrary, the sea surface temperature (SST) was measured at about 1 m below the
325 sea level using a high-accuracy conductivity and temperature recorder (SBE37/39; Sea Bird
326 Electronics) with an accuracy of 0.002 K. According to Donlon et al. (2002), there is a strong
327 correlation between body SST and skin SST. Although wind speed has a significant effect on this
328 relationship, a constant correction offset can be applied when the wind speed exceeds 6 m/s
329 (Alappattu et al., 2017). In fact, 83% of the samples had wind speeds above 4 m/s, and as
330 suggested by Vanhellemont (2020), the bulk SST measured at moored buoys can be adjusted to
331 the skin SST by using a correction offset of 0.17 K.

332 3.1.1.3 Calculation of other variables

333 Three variables, including e , D , and CI , were calculated with the RH, T_a , and R_g ,
334 measurements separately. Therefore, these three variables at hourly and daily scales were
335 obtained from the corresponding measurements. Specifically, the daily (hourly) mean e was
336 calculated from the daily (hourly) RH using the following equation:

$$337 \quad e = 6.1121 \frac{RH}{100} \exp\left(\frac{17.502T_a}{T_a + 240.97}\right) \quad (10)$$

338 Note that Equation (10) only works when T_a is in the range -30–50 °C (Buck, 1981), and
339 T_a should be in items of °C.

340 The daily (hourly) dew point depression D was calculated according to Josey (2003) and
341 Henderson-Sellers (1984) as:



342
$$D = 34.07 + 4157 / \ln(2.1718 \cdot 10^8 / e) - T_a \quad (11)$$

343 The clearness index (CI) is calculated as the ratio of the surface R_g to the extraterrestrial
344 solar radiation (DSR_{toa}) (Ogunjobi & Kim, 2004). CI generally represents the atmospheric
345 transmissivity affected by permanent gases, aerosols, and the optical thickness of the clouds
346 (Alados et al., 2012; Flerchinger et al., 2009; Gubler et al., 2012; Jiang et al., 2015; Meyers &
347 Dale, 1983), and it is widely used in radiation related researches (Iziomon et al., 2003; Jiang et
348 al., 2016; Jiang et al., 2015; Richard E Payne, 1972). The value of CI is between 0 and 1, where a
349 larger CI value represents a clearer sky. The hourly CI can be calculated as follows:

350
$$CI = \frac{R_g}{DSR_{toa}} \quad (12)$$

351 However, during nighttime, the hourly CI cannot be calculated by Equation (12) directly
352 because of a lack of R_g values; hence, it was calculated based on a 24-hour solar radiation
353 window centered on the hourly observation as suggested by Flerchinger et al. (2009). The daily
354 CI was calculated as the average of all hourly CI values in a day for the sake of considering
355 atmosphere variations at nighttime.

356 In this paper, CI was utilized to determine the condition as clear-sky when its value was
357 greater than 0.7 at both hourly and daily scales. Additionally, it was found that the cloud cover
358 derived from CI would help to improve the model performance after multiple experiments,
359 especially at nighttime. Therefore, CI was also used to calculate the cloud cover. Specifically, the
360 cloud fraction was linearly interpolated between $C = 1.0$ at a CI value of 0.4 for complete cloud
361 cover to $C = 0.0$ at a CI value of 0.7 for cloudless, both at daily and hourly scales according to
362 Flerchinger et al. (2009). Because of the different calculation of CI during daytime and
363 nighttime, the uncertainty in the calculated cloud cover was different; hence, the R_1 estimates at
364 the hourly scale were further examined at daytime and nighttime. Therefore, all meteorological
365 factors (RH, T_a , e , and D) at daily and at hourly scales were respectively prepared accordingly.

366 3.1.2 Cloud parameters from the ERA5 reanalysis data set

367 As described above, the cloud cover represented by the fraction (C) is usually taken into
368 account when estimating R_1 affected by clouds. However, in this study, two more cloud-related
369 parameters, including clw and ciw (see Table 1), from the ERA5 reanalysis product were also
370 considered in the modeling. The total amount of liquid water per unit area in the air column from
371 the base to the top of the cloud is called the total column cloud liquid water (clw), and its chilled
372 counterpart (ice) is called the total column cloud ice water (ciw) (Nandan et al., 2022). ERA5 is
373 the fifth generation atmospheric reanalysis product, and it was produced based on 4D-Var data
374 assimilation using the Integrated Forecasting System (IFS) with an enhanced spatial resolution
375 (0.25°) and time resolution (hourly) compared to its previous version ERA-interim (Hoffmann et
376 al., 2019) from 1979 to present. Clouds in ERA5 are represented by a fully prognostic cloud
377 scheme, in which cloud fractions and cloud condensates obey mass balance equations (Tiedtke,
378 1993). The ERA5 clw values are in good agreement with those obtained from radiosonde
379 observations (Nandan et al., 2022). Overall, relative to ERA-interim, ERA5 shows reduced
380 biases in the total ice water path versus other satellite-based observational products. Therefore,
381 the two cloud parameters were extracted from the locations of the 65 moored buoy sites directly
382 at the hourly scale, and then their daily means were calculated by averaging the 24 valid hourly
383 values. ERA5 cloud product is available on the Climate Data Store (CDS) cloud server
384 (<https://cds.climate.copernicus.eu/cdsapp#!search?type=dataset>).



385 Overall, 70% of the samples at each moored buoy site, including 33,151 daily samples
386 and 917,270 hourly samples, were randomly selected for new model training and calibration of
387 the eight previous models (Mod1–Mod8). The other 30% of the data at each site, including
388 14,115 daily samples and 358,038 hourly samples (daytime: 147,981; nighttime: 210,057), were
389 used for model validation.

390 3.2. Methodology

391 A new model that could estimate ocean-surface R_1 under all-sky conditions at both hourly
392 and daily scales was developed based on the moored measurements and ERA5 cloud parameters.
393 Moreover, the eight evaluated R_1 models were all recalibrated so as to evaluate the model's
394 accuracy objectively. Based on the corresponding validation samples, the R_1 values produced by
395 the nine models were compared under clear-sky and all-sky conditions at hourly and daily scales,
396 where the comparison at the hourly scale was further divided into daytime and nighttime values.

397 3.2.1 New R_1 estimation model development

398 As mentioned above, T_a and the humidity-related factors (e.g., RH) were enough to
399 characterize the variations in R_1 under clear-sky conditions. However, for cloudy skies, R_1 is
400 enhanced by the cloud base emitting (T Wang et al., 2020; Yang & Cheng, 2020). Cloud cover is
401 one of the most commonly used cloud-related parameters. In addition, theoretically, the cloudy-
402 sky R_1 is significantly influenced by the cloud's base temperature, which is determined by the
403 CBH; hence, CBH is thought to be necessary in determining R_1 under cloudy-sky conditions
404 (Viúdez-Mora et al., 2015). However, it is difficult to obtain the CBH accurately, especially for
405 partly cloudy skies (Zhou & Cess, 2001) because of the unavailability of the cloud's geometrical
406 thickness (Yang & Cheng, 2020). Therefore, other parameters that could provide information on
407 the CBH were explored. In the study of Hack (1998), a physical correlation between clw and
408 CBH was revealed for most cases, while clw was successfully used as an effective surrogate of
409 the CBH in the study of Zhou and Cess (2001). However, Zhou et al. (2007) pointed out that the
410 effects of ice clouds on R_1 should also be considered when the atmospheric water vapor is low or
411 at high latitudes, which means that ciw also needs to be taken into account. Inspired by these
412 studies, clw and ciw, both in logarithmic form, were introduced in the development of a new
413 model named Modnew, in which R_1 under all-sky conditions at the ocean surface was related to
414 five parameters including T_a , RH, clw, ciw, and C. Modnew was trained by the corresponding
415 training samples at hourly and daily scales. Details of the development of the new model
416 presented in the present study are given in Section 4.1.

417 3.2.2 Model performances evaluation

418 Table 4 lists the different cases for the R_1 model comparison. As shown in Table 4, the
419 nine evaluated models (Mod1–Mod8 and Modnew) were all used for clear-sky R_1 estimation at
420 both hourly and daily scales, while only four models (Mod6–Mod8 and Modnew) were evaluated
421 under all-sky conditions. Three metrics were employed to present the model accuracy: R^2 , the
422 root-mean-square error (RMSE), and bias. Generally, all three statistics were calculated to
423 evaluate the accuracy of different models, but the RMSE values had larger weights.

424 **Table 4**
425 *Detailed Information of the Six Cases Considered in the Model Evaluation*

Case	Training	Validation	Evaluated model
------	----------	------------	-----------------



		samples			
Clear-sky	Hourly	Daytime	176,510	40,805	Mod1-Mod8, Modnew
		Nighttime		35,125	Mod1-Mod8, Modnew
	Daily		3,443	1,447	Mod1-Mod8, Modnew
All-sky	Hourly	Daytime	917,270	147,981	Mod6-8, Modnew
		Nighttime		210,057	Mod6-8, Modnew
	Daily		33,151	14,115	Mod6-8, Modnew

426 4 Results and Analysis

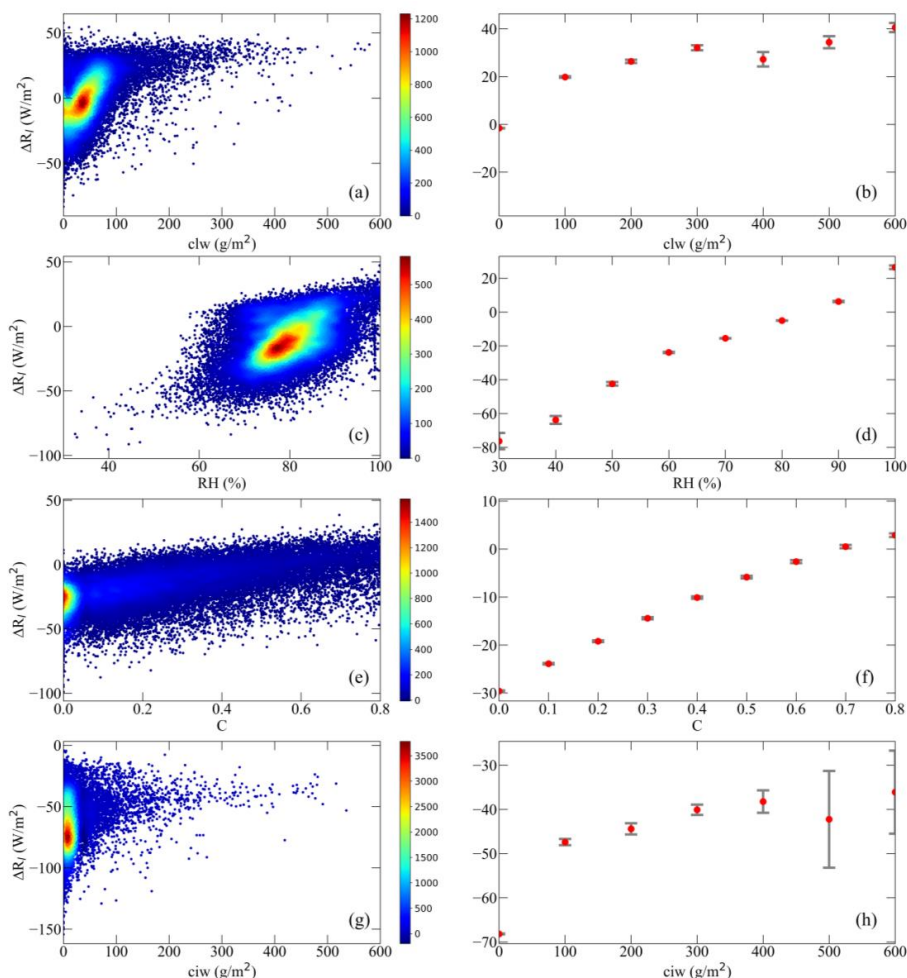
427 In this section, Modnew is introduced first, and then the validation results of the nine
 428 evaluated models under various cases are compared and analyzed. Lastly, further analyses are
 429 conducted on Modnew.

430 4.1 Modnew development

431 As mentioned above, the ocean-surface R_l in Modnew is related to five parameters (T_a ,
 432 clw , RH , C , and ciw) for hourly and daily scales under all-sky conditions. To understand better
 433 the contribution made by each variable on R_l , the five parameters were introduced into Modnew
 434 gradually. Taking the daily all-sky R_l as an example, R_l was first only characterized by the fourth
 435 power of T_a based on the Stefan–Boltzmann law as follows:

$$436 R_l = a_{new} \sigma T_a^4 + b_{new} \quad (13)$$

437 where a_{new} and b_{new} are empirical coefficients, determined as 0.85 and 14.96, respectively,
 438 based on the daily training samples. Then, the correlations between the model residuals in R_l
 439 (referred to as ΔR_l) that define the difference between the in situ R_l measurements and the R_l
 440 estimates from Equation (13) and other four parameters (clw , RH , C , and ciw) were explored one
 441 by one. The results are found in Figure 2.



442

443 **Figure 2.** The scatter plots between the model residuals, ΔR_1 , from Equation (13) and (a) clw, (c)
 444 RH, (e) C, and (g) ciw. Panels (b), (d), (f), and (h) are their corresponding box plots.

445 Figures 2(a), 2(c), 2(e), and 2(g) present scatter plots between ΔR_1 and clw, RH, C, and
 446 ciw, respectively. In order to show their relationships better, the corresponding box plots, in
 447 which the mean of ΔR_1 and its standard error (SEM) for each bin of the four parameters (in 10%
 448 increments) were calculated and presented in Figures 2(b), 2(d), 2(f), and 2(h), respectively.
 449 Specifically, ΔR_1 varied with clw and ciw in a logarithmic relationship (Figures 2(b) and 2(h),
 450 respectively), and with RH (Figure 2(d)) and C (Figure 2(f)) in approximately linear
 451 relationships. We found that by introducing the C, RH, clw and ciw in Equation (13) gradually,
 452 the RMSE error was reduced from 17.48 W/m² with Equation (13) to 12.61 W/m², 10.92 W/m²,
 453 10.11 W/m² and 9.87 W/m², and the level of R² increased accordingly from 0.64 to 0.81, 0.86,
 454 0.88 and 0.89, respectively. Hence, clw, RH, C, and ciw were introduced into Equation (13) in
 455 their appropriate forms and the final equation was taken as Modnew:

456

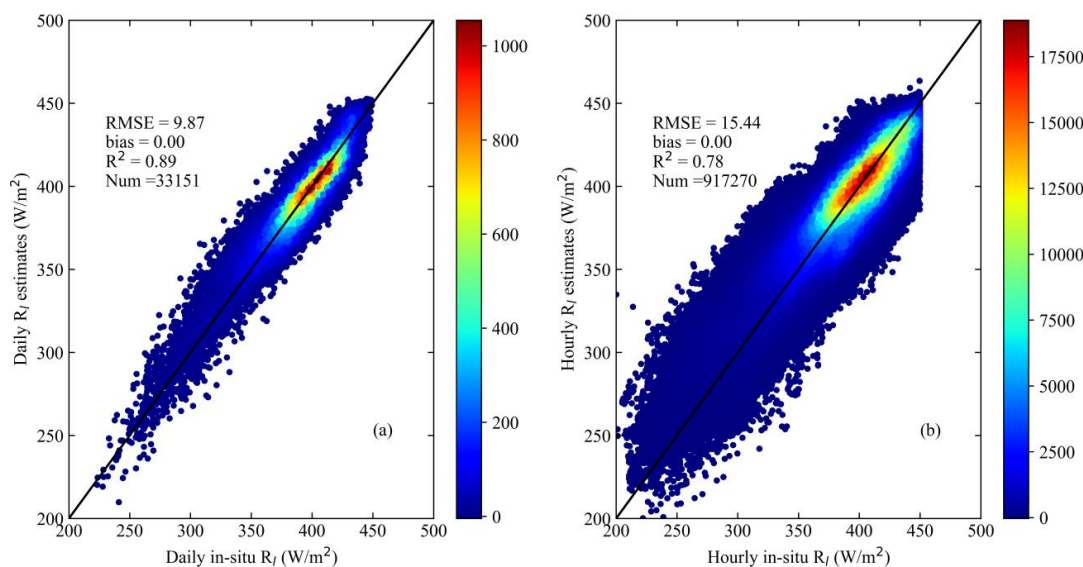
$$R_1 = a_{\text{new}} \sigma T_a^4 + b_{\text{new}} C + c_{\text{new}} \ln(1 + \text{clw}) + d_{\text{new}} \ln(1 + \text{ciw}) + e_{\text{new}} \text{RH} + f_{\text{new}}$$



457

(14)

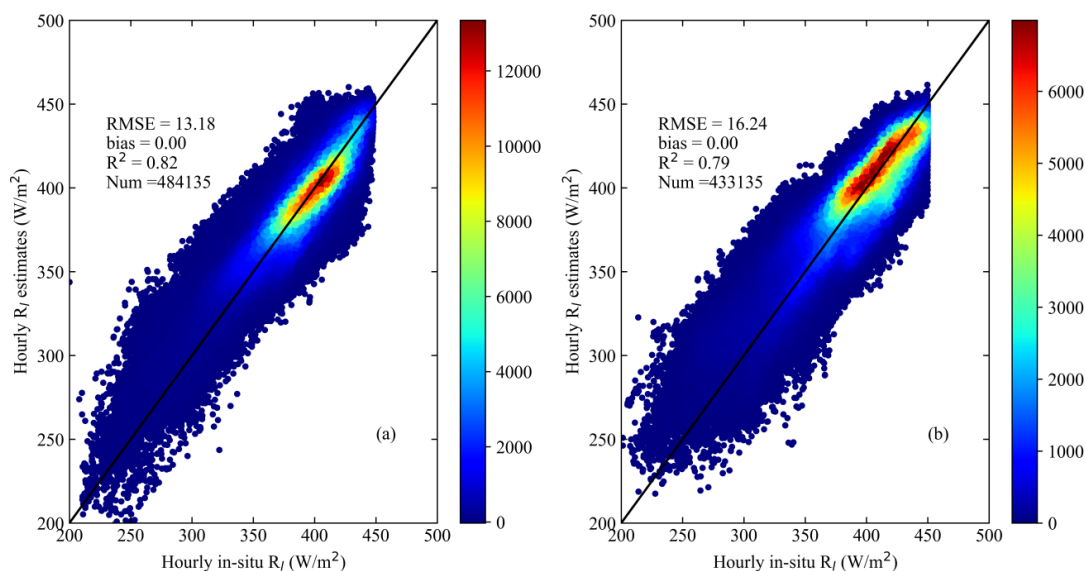
458 where a_{new} , b_{new} , c_{new} , d_{new} , e_{new} , and f_{new} are empirical coefficients. In this study, these
459 coefficients were determined as 1.06, 42.18, 4.90, -1.97, 0.89, and -178.28 respectively. Figure
460 3(a) shows that the overall training accuracy of the estimated all-sky ocean-surface R_1 from
461 Modnew was satisfactory, yielding an R^2 of 0.89, RMSE of 9.87 W/m^2 , and nearly no bias.
462 Afterwards, Equation (14) was used to determine the hourly ocean-surface R_1 based on the
463 corresponding hourly training samples (see Table 4). The hourly results shown in Figure 3(b)
464 were satisfactory, with an R^2 of 0.78, RMSE of 15.44 W/m^2 , and nearly no bias. Note that the R_1
465 measurements whose values were larger than 450 W/m^2 were thought to be unreasonable and
466 were manually removed (see Section 3.1).



467

468 **Figure 3.** Overall training accuracy of the all-sky daily R_1 at (a) daily and (b) hourly scales.

469 By considering the influence of the calculated cloud cover on the R_1 estimates, the hourly
470 results were separated into daytime and nighttime, respectively, as shown in Figure 4. The
471 training accuracy of the daytime sample was higher than that at nighttime, with R^2 values of 0.82
472 and 0.79 and RMSE values of 13.18 and 16.24 W/m^2 , respectively. It was assumed that the larger
473 uncertainties in the hourly ocean-surface R_1 at nighttime were possibly owing to the estimated
474 cloud cover, which might have an influence on Modnew in the form of overestimating R_1 .
475 Overall, the performance of Modnew was very good, both at daily and hourly scales for all-sky
476 R_1 estimation at the ocean surface.



477
 478 **Figure 4.** Overall training accuracy of the all-sky hourly R_f during (a) daytime and (b) nighttime.

479 **4.2 Model comparison results**

480 Based on the independent validation samples, Mod1–Mod8 and Modnew were validated
 481 one by one and compared for various cases (Table 4). Before that, the eight existing models were
 482 calibrated using the corresponding training samples, which means that Mod1–Mod5 were
 483 calibrated with the clear-sky training hourly/daily samples, while Mod6–Mod8 were calibrated
 484 with the all-sky training hourly/daily samples, i.e., the same as Modnew. Afterwards, these
 485 models were validated against the matched validation samples for each case. The updated
 486 coefficients of Mod1–Mod8 and the coefficients of Modnew for hourly and daily scales are
 487 given in Table 5. For better illustration, the comparison results are presented for clear- and all-
 488 sky conditions in the following paragraphs.

489 **Table 5**
 490 *Coefficients of the Nine Models Used for Hourly/Daily Ocean-surface R_f Estimation. The Values*
 491 *in Parentheses are the Uncertainties of the Fitted Parameters*

Models	a	b	c	d	e	f
Hourly						
Mod1	0.675($\pm 6 \times 10^{-4}$)	0.052($\pm 3 \times 10^{-4}$)	/	/	/	/
Mod2	0.246($\pm 1 \times 10^{-4}$)	7.77 $\times 10^{-4}$ (± 0.03)	/	/	/	/
Mod3	1.21($\pm 9 \times 10^{-5}$)	/	/	/	/	/
Mod4	1.056($\pm 8 \times 10^{-5}$)	/	/	/	/	/
Mod5	7.48(± 0.01)	1.28(± 0.003)	0.5(± 0.005)	/	/	/
Mod6	0.229($\pm 4 \times 10^{-4}$)	-0.006($\pm 8 \times 10^{-5}$)	/	/	/	/
Mod7	0.812($\pm 2 \times 10^{-4}$)	0.001($\pm 7 \times 10^{-6}$)	0.121($\pm 1 \times 10^{-4}$)	/	/	/
Mod8	-5.557(± 0.38)	13.378(± 0.35)	82.43(± 1.21)	0.85(± 0.02)	85.33(± 0.60)	/
Modnew	0.986($\pm 6 \times 10^{-4}$)	40.991(± 0.05)	3.116(± 0.01)	-2.478(± 0.01)	0.921(± 0.02)	-144.62(± 0.30)



<i>Daily</i>						
Mod1	0.65(±0.004)	0.06(±0.001)	/	/	/	/
Mod2	0.25(±0.003)	7.77×10 ⁻⁴ (±0.18)	/	/	/	/
Mod3	1.21(±5 ×10 ⁻⁴)		/	/	/	/
Mod4	1.061(±5 ×10 ⁻⁴)	/	/	/	/	/
Mod5	1.69(±0.09)	2.67(±0.25)	0.5(±0.02)	/	/	/
Mod6	0.286(±0.002)	-0.03(±3 ×10 ⁻⁴)	/	/	/	/
Mod7	0.805(±0.002)	0.002(±8 ×10 ⁻⁵)	0.133(±0.01)	/	/	/
Mod8	-0.34(±0.02)	8.545(±0.19)	-12.19(±0.59)	0.08(±0.009)	0.08(±0.006)	/
Modnew	1.06(±0.002)	42.18(±0.22)	4.90(±0.06)	-1.97(±0.04)	0.89(±0.008)	-178.28(±1.15)

492 4.2.1 Clear sky

493 All models, including the eight previous models (Mod1–Mod8), and the newly developed
 494 model (Modnew), could be used under clear-sky conditions at both hourly and daily scales with
 495 the updated coefficients given in Table 5.

496 4.2.1.1 Hourly scale

497 Table 6 shows the validation results of the nine models under clear-sky conditions at the
 498 hourly scale. Meanwhile, the validation results of Mod1–Mod8 with their original coefficients
 499 (see Section 2) are also presented in Table 6, using the same validation samples for comparison.

500 **Table 6**

501 *Overall Validation Accuracy of the Nine Ocean-surface R_l Models under Clear-sky Conditions at*
 502 *the Hourly Scale. The Values in Parentheses for Mod1–Mod8 are the Validation Results Found*
 503 *Using Their Original Coefficients*

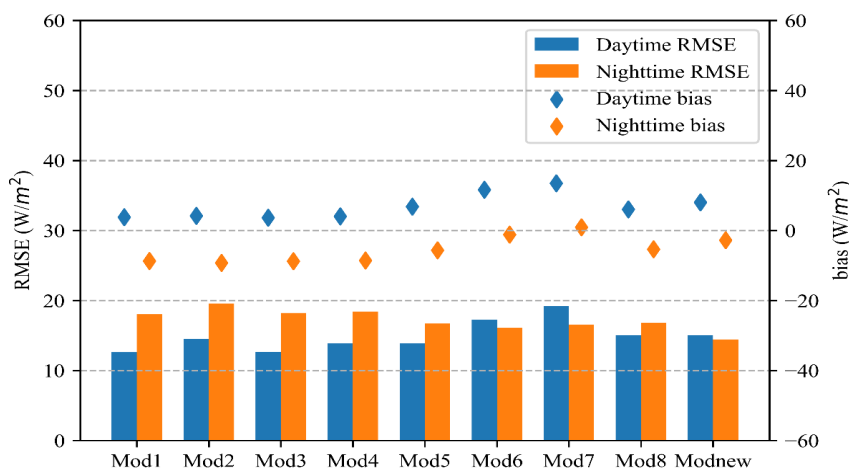
Models	R ²	RMSE(W/m ²)	bias(W/m ²)
Mod1	0.77 (0.78)	14.69 (15.43)	-0.42 (-0.88)
Mod2	0.71 (0.71)	16.37 (16.61)	-0.31 (-2.80)
Mod3	0.77 (0.77)	14.77 (17.87)	-0.53 (9.84)
Mod4	0.74 (0.74)	15.53 (17.11)	-0.22 (7.33)
Mod5	0.77 (0.77)	14.62 (26.90)	-0.44 (-19.56)
Mod6	0.75 (0.77)	16.87 (21.51)	7.33 (15.28)
Mod7	0.74 (0.77)	18.37 (17.52)	9.27 (-9.57)
Mod8	0.78 (0.78)	15.59 (37.00)	2.45 (-33.27)
Modnew	0.79	14.82	4.40

504 The validation results illustrate that most models estimated the clear-sky hourly ocean-
 505 surface R_l with a similar accuracy, with R² values ranging from 0.74 to 0.79, RMSE values
 506 ranging from 14.62 to 18.37 W/m², and bias values ranging from -0.53 to 9.27 W/m² (Table 6).
 507 All eight existing models with the calibrated coefficients had a higher accuracy than those with
 508 the original coefficients except Mod7; in particular, the RMSE of Mod8 decreased by ~21 W/m².
 509 The magnitude of the bias of Mod1–Mod8 also decreased after recalibration, with the
 510 magnitudes of the biases of Mod1–Mod5 being much smaller than those of Mod6–Mod8 and
 511 Modnew, which were trained with the all-sky hourly samples. Among the four all-sky models,
 512 the newly developed Modnew performed the best, with the largest R² of 0.79, the smallest
 513 RMSE of 14.82 W/m².

514 Then, the hourly validation results of the nine models were further examined using the



515 daytime and nighttime values separately, which are shown in Figure 5. The performance of most
516 models, including the five clear-sky models (Mod1–Mod5) and one all-sky model (Mod8), in
517 estimating the hourly clear-sky R_1 during the daytime was much better than that at nighttime,
518 with RMSE values at daytime and nighttime ranging from ~ 12.50 to 15.06 W/m^2 and 16.80 to
519 19.50 W/m^2 , respectively. On the contrary, the performances of Mod6–Mod7 and Modnew were
520 better at nighttime than that at daytime, with RMSE values at daytime and nighttime ranging
521 from ~ 15.00 to 19.20 W/m^2 and 14.40 to 16.60 W/m^2 , respectively. Regarding the bias values, at
522 nighttime, all five clear-sky models had a significant underestimation problem (negative biases),
523 while the all-sky models had smaller bias values. This may be due to the uncertainty in the
524 calculated CI at nighttime, which could influence the cloud determination and then R_1 . In
525 addition, among the five clear-sky models, Mod2 based only on air temperature shows the lowest
526 accuracy in terms of RMSE during both daytime and nighttime. Among the nine models,
527 Modnew had the most stable performance in hourly R_1 estimation under clear-sky conditions
528 during both daytime and nighttime with similar RMSE values of 15.03 and 14.38 W/m^2 ,
529 respectively, where in particular its nighttime R_1 estimation accuracy was the best among the nine
530 models.



531
532 **Figure 5.** Validation accuracy of the estimated R_1 under clear-sky conditions at the hourly scale
533 for the nine models represented by RMSE (left axis) and bias (right axis).

534 Furthermore, the four all-sky R_1 estimation models (Mod6–Mod8 and Modnew) were also
535 trained using the clear-sky hourly samples, and their outputs were validated against the in situ
536 observations. The estimation accuracy of the four all-sky models all improved after calibration:
537 their overall validated RMSE values decreased to ~ 13.40 to 15.40 W/m^2 and ~ 12.01 to 14.29
538 W/m^2 during the daytime, slight decreases (~ 1 W/m^2) at nighttime, and their biases values tended
539 to 0. This indicates that the ability of the four all-sky models in estimating clear-sky hourly R_1
540 was comparable with or even better than the other five models which only work for clear-sky
541 conditions. Indeed, Modnew performed the best of all models during either daytime or nighttime,
542 with corresponding validated RMSE values of 12.01 and 16.00 W/m^2 , respectively.

543 4.2.1.2 Daily scale

544 As for the results at the daily scale, the nine evaluated models were trained with the



545 corresponding daily training samples (see Table 4) and validated against the in situ
 546 measurements. As shown in Table 7, the estimation accuracy of the daily clear-sky ocean-surface
 547 R_1 from nearly all previous models improved significantly after recalibration, where the RMSE
 548 values and the magnitudes of the bias decreased by up to ~ 4 W/m² and ~ 9 W/m², respectively,
 549 except for Mod7. The five clear-sky models (Mod1–Mod5) performed much better than the three
 550 previous all-sky models (Mod6–Mod8), with RMSE values ranging from 9.58 to 11.43 W/m² and
 551 14.02 to 15.69 W/m², and biases values ranging from 0.11 to 0.57 W/m² and 4.99 to 9.53 W/m²,
 552 respectively. Besides, the Mod2 still exhibited lower accuracy than the other four clear-sky
 553 models, with the highest validated RMSE value of 11.43 W/m². The performance of Modnew
 554 was the best among the four all-sky models, with the smallest validated RMSE value of 10.76
 555 W/m² and bias of 3.53 W/m². Similar to the hourly results under the clear-sky conditions, the
 556 validation results improved considerably if all four all-sky models were trained using the clear-
 557 sky daily samples: their RMSE values and biases decreased to ~ 8 – 13 W/m² and were nearly
 558 zero, respectively, which were even better than the corresponding decreases measured for Mod1
 559 to Mod5. Modnew was the best in comparison to the other three all-sky models, in this case
 560 yielding an RMSE of 8.36 W/m².

561 **Table 7**
 562 *Overall Validation Accuracy of the Nine Ocean-surface R_1 Models under Clear-sky Conditions at*
 563 *the Daily Scale. The Values in Parentheses for Mod1–Mod8 are the Validation Results Found*
 564 *Using Their Original Coefficients*

Models	R ²	RMSE(W/m ²)	bias(W/m ²)
Mod1	0.89 (0.90)	9.66 (11.16)	0.38 (-2.00)
Mod2	0.85(0.85)	11.43 (11.91)	0.45 (-3.35)
Mod3	0.90(0.90)	9.87 (13.57)	0.11 (9.06)
Mod4	0.88(0.88)	10.50 (12.62)	0.57 (7.16)
Mod5	0.89 (0.89)	9.58 (11.92)	0.39 (6.97)
Mod6	0.87 (0.88)	14.32 (18.43)	9.53 (15.26)
Mod7	0.87 (0.88)	14.02 (13.67)	8.15 (-9.18)
Mod8	0.80 (0.81)	15.69 (19.63)	4.99 (-12.56)
Modnew	0.89	10.76	3.53

565 In summary, for the ocean-surface R_1 estimation under clear-sky conditions, the use of an
 566 all-sky model trained with the clear-sky samples is recommended at both hourly and daily scales.
 567 Modnew performed the best of all nine models when trained with the clear-sky samples, and was
 568 comparable with the other five clear-sky models when trained with the all-sky samples.
 569 Furthermore, our validation results show that the accuracy of Mod2 is not as high as that of other
 570 clear-sky models that include water vapor variable in terms of RMSE.

571 4.2.2 All sky

572 4.2.2.1 Hourly scale

573 Table 8 gives the overall validation results of the all-sky hourly scale ocean-surface R_1
 574 from the four models against the independent validation samples with the updated and original
 575 coefficients, respectively.

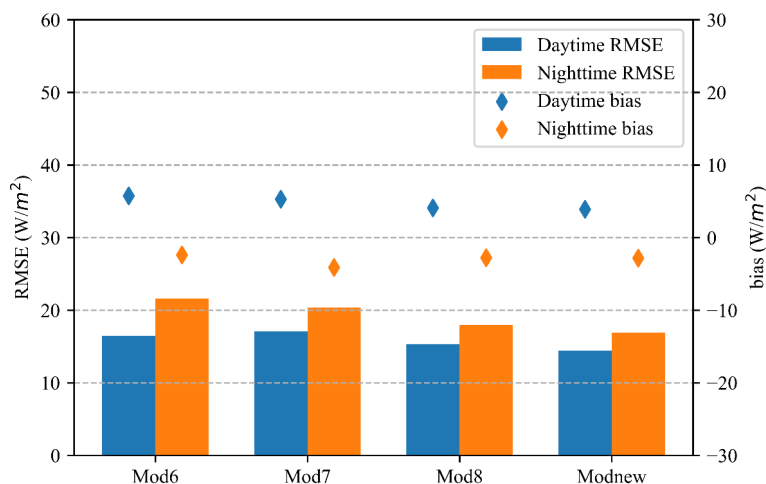
576 **Table 8**



577 *Overall Validation Accuracy of Four Ocean-surface R_1 Models under All-sky Conditions at the*
 578 *Hourly Scale. The Values in Parentheses for Mod6–Mod8 are the Validation Results Found*
 579 *Using Their Original Coefficients*

Models	R^2	RMSE(W/m ²)	bias(W/m ²)
Mod6	0.67 (0.65)	18.53 (19.84)	0.05 (3.83)
Mod7	0.66 (0.64)	19.06 (26.10)	-0.14 (-10.27)
Mod8	0.74 (0.51)	16.91 (37.33)	-0.41 (-28.47)
Modnew	0.76	15.95	-0.04

580 Compared to the results in Table 6, the estimation accuracies under all-sky conditions
 581 shown in Table 8 were generally worse, with lower R^2 values (0.66–0.76) and bigger RMSE
 582 values (15.95–19.06 W/m²), which indicates that the uncertainty in the cloud information was the
 583 major reason for the increased uncertainty in the R_1 estimation. As in previous results, the three
 584 previous models, Mod6–Mod8, performed much better after recalibration, with decreased RMSE
 585 values up to ~20 W/m² and their bias values tended to 0; Mod7 still performed the worse.
 586 Modnew performed the best, with an RMSE of 15.95 W/m² and a bias of -0.04W/m², followed
 587 by Mod8.



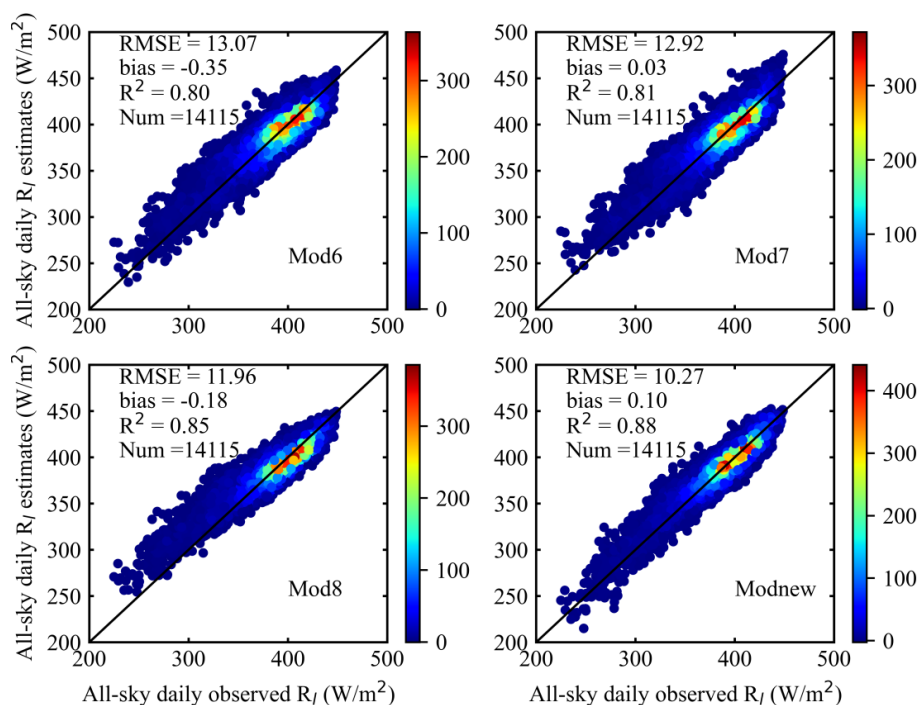
588 **Figure 6.** Validation accuracy of the estimated R_1 under all-sky conditions at the hourly scale for
 589 Mod6-Mod8 and Modnew represented by RMSE (left axis) and bias (right axis).
 590

591 The hourly results in Table 8 were examined for daytime and nighttime values, as shown
 592 in Figure 6. The results show that the estimation accuracies of the four models were overall
 593 better during the daytime than at nighttime, with smaller RMSE values for the former.
 594 Specifically, during daytime hours, the accuracy of Modnew was similar to that of Mod8, with
 595 RMSEs of 14.43 and 15.33 W/m², respectively, which were better than those of Mod6 and
 596 Mod7, which yielded RMSEs of 16.46 and 17.09 W/m², respectively. However, Mod7 performed
 597 a little bit better than Mod6 during the nighttime, although its overall performance was the worst.
 598 It is speculated that the larger uncertainties in the all-sky ocean-surface R_1 values at nighttime
 599 can possibly be attributed to the cloud information at nighttime, which was difficult to estimate
 600 accurately compared to the daytime cloud information.



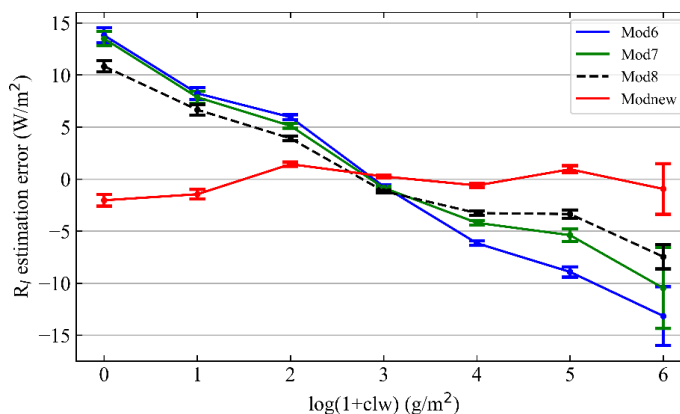
601 4.2.2.2 Daily scale

602 Figure 7 shows the overall validation accuracies of the all-sky daily ocean-surface R_1
603 values from the four models. Compared with Mod6–Mod8, Modnew had the best performance,
604 with an validated RMSE of 10.27 W/m^2 , a bias of 0.10 W/m^2 , and an R^2 of 0.88, followed by
605 Mod8, which yielded an RMSE of 11.96 W/m^2 , a bias of -0.18 W/m^2 , and an R^2 of 0.85.
606 However, Mod8 had a tendency to overestimate low values ($<300 \text{ W/m}^2$), as did Mod6 and
607 Mod7.



608
609 **Figure 7.** Overall validation result of the calculated all-sky daily ocean-surface R_1 from the four
610 models against the independent moored measurements.

611 Overall, it is speculated that Modnew performed better than Mod6–Mod8 because of the
612 introduction of two cloud-related parameters (clw and ciw) into the model in addition to the
613 cloud fraction. In order to demonstrate this speculation better, the relationship between the
614 estimation errors in the daily all-sky ocean-surface R_1 of the four models and clw , which was
615 used to represent the CBH, was further analyzed. The corresponding mean of the estimation
616 errors in the daily all-sky ocean-surface R_1 and its SEM for each bin of clw in logarithmic format
617 (in 10% increments) were calculated, as presented in Figure 8.



618

619 **Figure 8.** The averaged R_1 estimation errors and its SEM of Mod6 – Mod8 and Modnew varied
620 with clw in logarithmic format.

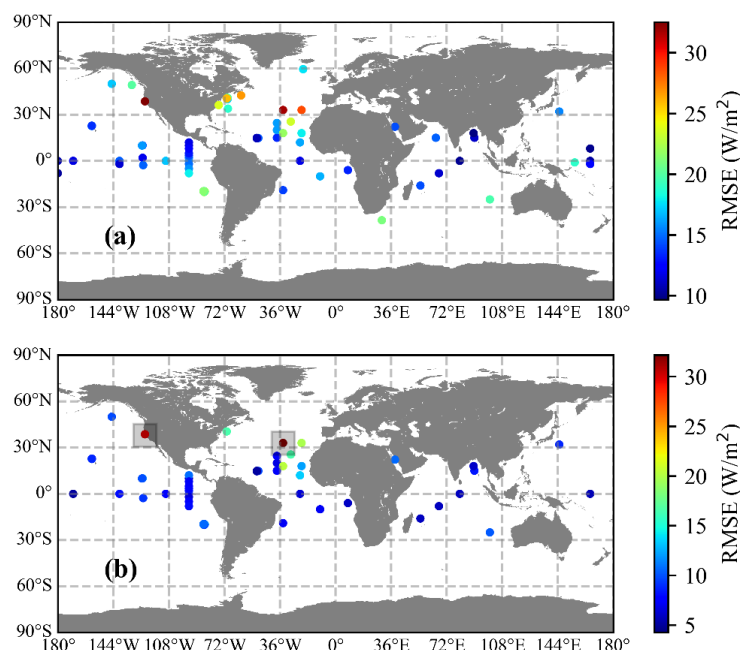
621 From the results in Figure 8 it can be seen that the R_1 estimation errors of Mod6–Mod8
622 were negative linearly related to increasing $\log(1+clw)$; such behavior is not seen for Modnew.
623 This indicates that the cloud information related to the variations in daily ocean-surface R_1 are
624 not fully characterized by only the cloud fraction. Although Mod8 performed better than Mod6
625 and Mod7 because of the introduction of the dew point depression to compensate for the
626 difference between the surface temperature and cloud base temperature, the contributions of the
627 cloud base emission to R_1 still cannot be thoroughly expressed over the ocean surface. Hence,
628 Modnew performed superior to other models because it also takes clw as input. Moreover, ciw
629 was also introduced in Modnew to ensure its robust performance at high latitudes.

630 4.3 Further analysis on Modnew

631 Based on the direct validation results described above, Modnew satisfactorily estimated
632 the ocean-surface R_1 under both clear- and all-sky conditions at both hourly and daily scales.
633 Hence, further analysis of this new model, such as testing its performance robustness and a
634 sensitivity analysis, was conducted, and the results are given below.

635 4.3.1 Modnew performance analysis

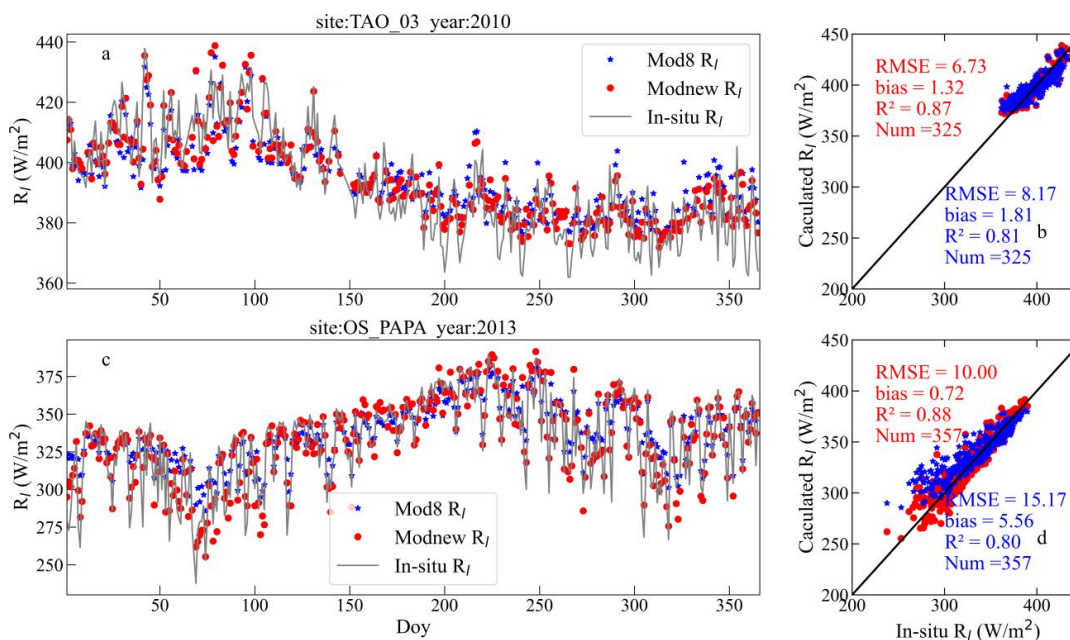
636 In order to examine the robustness of its performance, the spatial distributions of the
637 validation accuracies of the all-sky R_1 estimates from Modnew at the moored buoy sites are
638 presented in Figures 9(a–b) for hourly and daily scales, respectively. Note that the moored buoy
639 data from which the number of provided validation samples were less than 50 were excluded to
640 provide a more objective comparison.



641

642 **Figure 9.** Validation accuracies of Modnew on the hourly scale (a) and daily scale (b) at different
643 sites represented by the RMSE values. The two moored buoys in the shaded boxes in (b) are
644 UOP_SMILE88 (38°N, 123.5°W) and UOP_SUB_NW (33°N, 34°W).

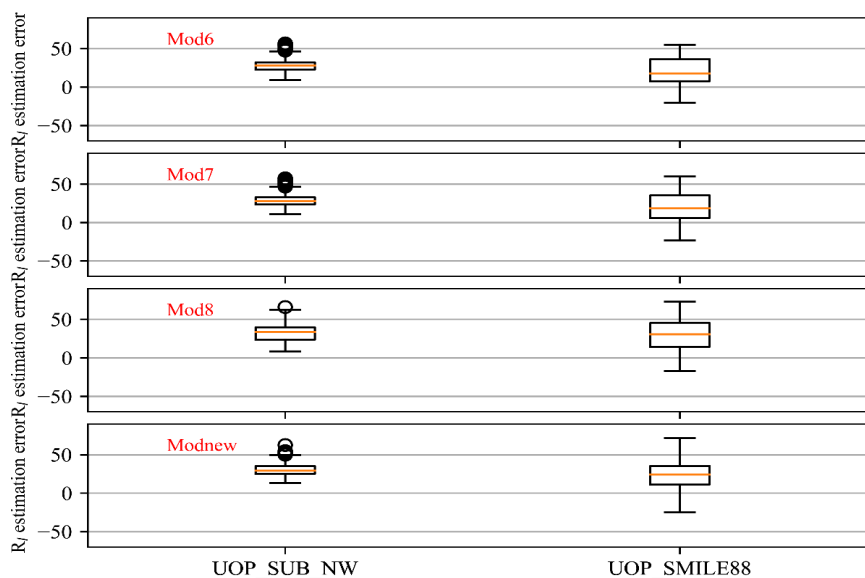
645 The spatial distribution of the validation accuracy (represented by RMSE) of the R_1
646 estimates from Modnew was similar for the hourly and daily data. Their RMSE values got larger
647 from tropical to the high latitude seas, although the daily R_1 estimates were generally more
648 accurate than the hourly ones, and the validation accuracy for sites at open seas was more
649 accurate than that within coastal seas. For a better illustration, two time series of the estimated
650 daily ocean-surface R_1 from Modnew at two sites were randomly selected and shown in Figure
651 10, and the one from Mod8 was added for comparison, as well as the corresponding scatter plots.
652 The two buoys, TAO_03 (0°N, 140°W) and OS_PAPA (50°N, 145°W), are in equatorial and
653 mid-high latitude seas, respectively. The temporal variations in the all-sky daily R_1 estimates
654 from the two models both captured the variations in the moored R_1 measurements very well, but
655 the ones from Modnew were closer to the measurements at high values and low values,
656 especially at the OS_PAPA site. The validation accuracy of Modnew was higher than that of
657 Mod8 at both sites, and Modnew performed better for tropical seas, with validated RMSE values
658 of 6.73 and 10.00 W/m^2 , respectively, which was assumed that more samples used for modeling
659 were collected at tropical seas and this would influence the model performance at mid-high
660 latitude seas.



661

662 **Figure 10.** Time series and scatter plots of the R_1 estimates and the moored R_1 measurements at
663 the (a–b) TAO_03 ($0^\circ N$, $140^\circ W$) and (c–d) OS_PAPA ($50^\circ N$, $145^\circ W$) sites. The red points and
664 blue points represent Modnew and Mod8, respectively.

665 However, it was noted that Modnew performed poor at some sites, such as
666 UOP_SMILE88 ($38^\circ N$, $123.5^\circ W$) and UOP_SUB_NW ($33^\circ N$, $34^\circ W$) (see the shaded boxes in
667 Figure 9). The estimation errors in the daily R_1 from Modnew at the two moored buoys were
668 calculated, as shown in Figure 11, and the ones from the other three all-sky models, Mod6–
669 Mod8, are shown for comparison. It can be seen that the four evaluated all-sky models all
670 worked poorly at the two sites, all giving overestimations. A possible explanation may be
671 attributed to the differences in the characteristics of the atmospheric boundary layer over the two
672 sites relative to the open sea. Specifically, UOP_SMILE88 is deployed on the northern California
673 shelf, which is influenced by air temperature inversions (ATIs) (Dorman et al., 1995), and
674 UOP_SUB_NW is deployed near the eastern flank of the Azores anticyclone system (Moyer &
675 Weller, 1997). As such, the atmospheric conditions of the two sites are different from those over
676 the open sea, which would affect the estimation of R_1 made with models whose coefficients were
677 determined by samples collected mostly from sites located in the open sea. Therefore, more
678 samples should be collected within these seas to help to improve the ocean-surface R_1 estimation
679 accuracy in these areas.



680

681 **Figure 11.** Box plots of the R_1 estimation errors from models Mod6, Mod7, Mod8, and Modnew
 682 at UOP_SMILE88 (38°N, 123.5°W) and UOP_SUB_NW (33°N, 34°W).

683 4.3.2 Sensitivity analysis

684 In order to quantify the impact of each parameter on the calculated R_1 in Modnew, the
 685 SimLab software (<http://simlab.jrc.ec.europa.eu>) was used to conduct a global sensitivity
 686 analysis. All inputs in Modnew (T_a , RH, C, clw, and ciw) were entered into the software
 687 separately, and then 2,000 ocean-surface R_1 values were calculated using Modnew by taking
 688 2,000 combinations of these parameters as inputs. Afterwards, the Fourier amplitude sensitivity
 689 test (FAST) method (Saltelli et al., 1999) in the SimLab software was employed to conduct a
 690 sensitivity analysis based on the inputs, and the corresponding estimated R_1 values were used for
 691 a sensitivity analysis using the total sensitivity index (TSI). The TSI indicates each parameter's
 692 total contribution to the output variance when the interactions of other parameters are also
 693 considered, and was used to quantify the sensitivity of each parameter. Table 9 shows the TSI of
 694 each parameter in Modnew. Specifically, T_a had the most important effect on R_1 with the largest
 695 TSI of 41.26%, followed by C (25.6%) and RH (21%). Therefore, the performance of Modnew
 696 mainly depended on the accuracy of the T_a , C, and RH. The TSI of clw was the fourth highest
 697 with 8%, but it is essential to supplement cloud information that cloud cover alone cannot
 698 provide, especially for cloud-sky conditions. In terms of ciw, its TSI was just 0.008, which was
 699 possibly because only a few samples at high-latitudes were used in this study.

700 **Table 9**

701 *FAST Sensitivity Indices of the First Order for Each Input Variable in Modnew*

T_a	RH	C	Clw	ciw
0.4126	0.21	0.256	0.08	0.008

702



703 5 Conclusions

704 Due to the significance of R_1 at the ocean surface, many empirical models have been
705 established for ocean-surface R_1 calculation based on observations by relating R_1 to some climatic
706 factors, such as T_a , RH, and so on. However, most models were developed only for clear days,
707 and for those models that can calculate the all-sky R_1 , only the cloud cover is taken into account,
708 which is thought to be insufficient for characterizing the influence of clouds on R_1 , especially for
709 ocean surfaces where cloudy skies are common. Indeed, most previous R_1 estimation models
710 were developed only within a specific region based on limited observations, and some for just
711 land surfaces. Consequently, there was a need to perform comprehensive evaluations of these
712 models, including their ability to predict R_1 over global seas.

713 In this study, a new model called Modnew, in which the all-sky ocean-surface R_1 is
714 nonlinearly related to T_a , RH, C, clw, and ciw, has been successfully developed. This model, as
715 well as eight comparison models, was used to estimate the all-sky ocean-surface R_1 at both
716 hourly and daily scales based on comprehensive observations collected from 65 globally
717 distributed moored buoys from 1988 to 2019. In contrast to previous models, Modnew
718 incorporates more cloud-related parameters (i.e., clw and ciw) into the model besides just cloud
719 cover. Modnew and the eight previous R_1 models were assessed against the moored values for
720 various cases, including clear- and all-sky conditions at daytime and nighttime and at hourly and
721 daily scales. After careful analysis, several major conclusions could be drawn, as follows:

722 (1) The eight previous models performed much better after calibration of their
723 coefficients with the global observations for almost all cases, except Mod7 in some situations.

724 (2) For the clear-sky ocean-surface R_1 estimation, the four all-sky models (Mod6–Mod8
725 and Modnew) could work comparably to or even better than the five clear-sky models (Mod1–
726 Mod5) if their coefficients were calibrated by the clear-sky samples, yielding overall validated
727 RMSE values ranging from 13.40 to 15.40 W/m^2 at the hourly scale and 8.00–13.00 W/m^2 at the
728 daily scale. In terms of daytime and nighttime, all five clear-sky models (Mod1–Mod5)
729 performed better at daytime than that at nighttime, and vice versa for the four all-sky models
730 except Mod7. Mod1–Mod5 generally had the tendency to underestimate R_1 at nighttime because
731 they do not consider the influence of clouds. Among all models, Modnew was the most robust,
732 yielding RMSE values of 15.03 W/m^2 and 14.38 W/m^2 at daytime and nighttime for the hourly
733 scale, respectively.

734 (3) For the all-sky ocean-surface R_1 estimation, the performance of the four evaluated
735 models was generally worse compared to that under clear-sky conditions, which further
736 demonstrated that the uncertainty in the all-sky R_1 estimation was highly dependent on accurate
737 cloud information. Specifically, at the hourly scale, the validated RMSE values of the four
738 models ranged from 15.95 to 19.06 W/m^2 , with better performance at daytime. At the daily scale,
739 the RMSE values ranged from 10.27 to 13.07 W/m^2 . Modnew also performed the best in these
740 cases, with an overall validated RMSE of 15.95 and 10.27 W/m^2 and bias values of -0.04 and
741 0.10 W/m^2 , respectively. It is worth noting that Modnew performed similarly during both
742 daytime and nighttime at the hourly scale.

743 In summary, the performance of Modnew was superior to other previous models for
744 ocean-surface R_1 estimation for any case, which was mainly because of the introduction of more
745 cloud-related information (clw and ciw). Further analysis of Modnew illustrated the significance
746 of the two parameters as well as cloud cover. However, all results again emphasized that the



747 accuracy of nearly all the empirical models was highly dependent on the spatial distribution,
748 quality, and quantity of the samples used for modeling. For instance, Modnew worked better at
749 open seas in tropical regions where more samples were available compared to other regions.
750 Therefore, many more samples at different regions, such as in coastal regions and high-latitude
751 seas, should be collected in the future to improve model performance. Moreover, more accurate
752 cloud information especially at nighttime is essential to decrease the uncertainty in the estimated
753 R_1 at the ocean surface.

754 **Competing interests**

755 The contact author has declared that none of the authors has any competing interests.

756 **Acknowledgments**

757 We acknowledge the buoy data sets provided by UOP, GTMBA, and OceanSITES
758 project. We are grateful to ECMWF for providing the reanalysis data sets. We would also like to
759 thank the contributions made by the anonymous reviewers and editor that helped improve the
760 quality of this paper.

761 **Funding**

762 This work was supported by the Natural Science Foundation of China (41971291).

763 **Data availability**

764 All data sets used in this research, including the moored buoy observations and satellite
765 and reanalysis data are publicly available. Detailed information on these data sets, including
766 citations and web links, is presented in Section 3.

767 **Author contributions.**

768 PJH and BJ designed and performed the study. All authors contributed to the analysis of
769 results and final version of the paper.

770 **References**

- 771 Aase, J. K., & S. B. Idso (1978), A comparison of two formula types for calculating long-wave radiation from the
772 atmosphere, *Water Resour Res*, 14(4), 623-625, <https://doi.org/10.1029/WR014i004p00623>.
773 Alados, I., I. Foyo-Moreno, & L. Alados-Arboledas (2012), Estimation of downwelling longwave irradiance under
774 all-sky conditions, *Int J Climatol*, 32(5), 781-793, <https://doi.org/10.1002/joc.2307>.
775 Alappattu, D. P., Q. Wang, R. Yamaguchi, R. J. Lind, M. Reynolds, & A. J. Christman (2017), Warm layer and cool
776 skin corrections for bulk water temperature measurements for air-sea interaction studies, *J Geophys Res-Oceans*,
777 122(8), 6470-6481, <https://doi.org/10.1002/2017jc012688>.
778 Bignami, F., S. Marullo, R. Santoleri, & M. E. Schiano (1995), Longwave radiation budget in the Mediterranean
779 Sea, *J Geophys Res-Oceans*, 100(C2), 2501-2514, <https://doi.org/10.1029/94jc02496>.
780 Bilbao, J., & A. H. de Miguel (2007), Estimation of Daylight Downward Longwave Atmospheric Irradiance under
781 Clear-Sky and All-Sky Conditions, *J. Appl. Meteor. Climatol.*, 46(6), 878-889, <https://doi.org/10.1175/jam2503.1>.



- 782 Boulrès, B., R. Lumpkin, M. J. McPhaden, F. Hernandez, P. Nobre, E. Campos, et al. (2008), The PIRATA
783 program: History, accomplishments, and future directions, *Bull. Amer. Meteor. Soc.*, 89(8), 1111-1126,
784 <https://doi.org/10.1175/2008bams2462.1>.
- 785 Brunt, D. (1932), Notes on radiation in the atmosphere, *Quart J Roy Meteor Soc*, 58, 389-420.
- 786 Brutsaert, W. (1975), On a derivable formula for longwave radiation from clear skies, *Water Resour Res*, 11(5),
787 742-744, <https://doi.org/10.1029/WR011i005p00742>.
- 788 Buck, A. L. (1981), New equations for computing vapor pressure and enhancement factor, *J Appl Meteorol*, 20(12),
789 1527-1532, [https://doi.org/10.1175/1520-0450\(1981\)020<1527:NEFCVP>2.0.CO;2](https://doi.org/10.1175/1520-0450(1981)020<1527:NEFCVP>2.0.CO;2).
- 790 Caniaux, G. (2005), A 1 year sea surface heat budget in the northeastern Atlantic basin during the POMME
791 experiment: 1. Flux estimates, *J. Geophys. Res.*, 110(C7), <https://doi.org/10.1029/2004jc002596>.
- 792 Centurioni, L. R., J. Turton, R. Lumpkin, L. Braasch, G. Brassington, Y. Chao, et al. (2019), Global in situ
793 observations of essential climate and ocean variables at the air–sea interface, *Front Mar Sci*, 6, 419,
794 <https://doi.org/10.3389/fmars.2019.00419>.
- 795 Clark, N. E., L. Eber, R. M. Laurs, J. A. Renner, & J. F. T. Saur (1974), Heat exchange between ocean and
796 atmosphere in the eastern North Pacific for 1961–71, *Tech. Rep. NMFS SSRF-682*, NOAA, U.S. Dept. of Commer.,
797 Washington, D. C.
- 798 Cleugh, H. A., R. Leuning, Q. Mu, & S. W. Running (2007), Regional evaporation estimates from flux tower and
799 MODIS satellite data, *Remote Sens Environ*, 106(3), 285-304, <https://doi.org/10.1016/j.rse.2006.07.007>.
- 800 Cottier, F. R., F. Nilsen, M. E. Inall, S. Gerland, V. Tverberg, & H. Svendsen (2007), Wintertime warming of an
801 Arctic shelf in response to large-scale atmospheric circulation, *Geophys Res Lett*, 34(10),
802 <https://doi.org/10.1029/2007GL029948>.
- 803 Cronin, M. F., C. L. Gentemann, J. Edson, I. Ueki, M. Bourassa, S. Brown, et al. (2019), Air-sea fluxes with a focus
804 on heat and momentum, *Front Mar Sci*, 6, <https://doi.org/10.3389/fmars.2019.00430>.
- 805 Deremble, B., N. Wienders, & W. K. Dewar (2013), CheapAML: A simple, atmospheric boundary layer model for
806 use in ocean-only model calculations, *Mon. Wea. Rev.*, 141(2), 809-821, <https://doi.org/10.1175/MWR-D-11-00254.1>.
- 807
- 808 Diak, G. R., W. L. Bland, J. R. Mecikalski, & M. C. Anderson (2000), Satellite-based estimates of longwave
809 radiation for agricultural applications, *Agr Forest Meteorol*, 103(4), 349-355, [https://doi.org/10.1016/S0168-1923\(00\)00141-6](https://doi.org/10.1016/S0168-1923(00)00141-6).
- 810
- 811 Doelling, D. R., N. G. Loeb, D. F. Keyes, M. L. Nordeen, D. Morstad, C. Nguyen, et al. (2013), Geostationary
812 enhanced temporal interpolation for CERES flux products, *J. Atmos. Oceanic Technol.*, 30(6), 1072-1090,
813 <https://doi.org/10.1175/JTECH-D-12-00136.1>.
- 814 Donlon, C. J., P. J. Minnett, C. Gentemann, T. J. Nightingale, I. J. Barton, B. Ward, & M. J. Murray (2002), Toward
815 improved validation of satellite sea surface skin temperature measurements for climate research, *J. Climate*, 15(4),
816 353-369, [https://doi.org/10.1175/1520-0442\(2002\)015<0353:tivoss>2.0.co;2](https://doi.org/10.1175/1520-0442(2002)015<0353:tivoss>2.0.co;2)
- 817 Dorman, C. E., A. G. Enriquez, & C. A. Friehe (1995), Structure of the lower atmosphere over the northern
818 California coast during winter, *Mon. Wea. Rev.*, 123(8), 2384-2404, [https://doi.org/10.1175/1520-0493\(1995\)123<2384:SOTLAO>2.0.CO;2](https://doi.org/10.1175/1520-0493(1995)123<2384:SOTLAO>2.0.CO;2).
- 819
- 820 Douville, H., J. F. Royer, & J. F. Mahfouf (1995), A new snow parameterization for the Meteo-France climate
821 model, *Climate Dynam*, 12(1), 21-35, <https://doi.org/10.1007/BF00208760>.
- 822 Dubois, C., S. Somot, S. Calmanti, A. Carillo, M. Déqué, A. Dell’Aquila, et al. (2012), Future projections of the
823 surface heat and water budgets of the Mediterranean Sea in an ensemble of coupled atmosphere–ocean regional
824 climate models, *Climate Dynam*, 39(7), 1859-1884, <https://doi.org/10.1007/s00382-011-1261-4>.
- 825 Ellington, R. G. (1995), Surface longwave fluxes from satellite observations: A critical review, *Remote Sens*
826 *Environ*, 51(1), 89-97, [https://doi.org/10.1016/0034-4257\(94\)00067-W](https://doi.org/10.1016/0034-4257(94)00067-W).
- 827 Fasullo, J. T., J. Kiehl, K. E. Trenberth, & J. T. Fasullo (2009), Earth’s Global Energy Budget, *Bull. Amer. Meteor.*
828 *Soc.*, 90(3), 311-324, <https://doi.org/10.1175/2008BAMS2634.1>
- 829 info:doi/10.1175/2008BAMS2634.1.
- 830 Flerchinger, G. N., W. Xaio, D. Marks, T. J. Sauer, & Q. Yu (2009), Comparison of algorithms for incoming
831 atmospheric long-wave radiation, *Water Resour Res*, 45(3), <https://doi.org/10.1029/2008wr007394>.
- 832 Freitag, H. P. (1994), Calibration procedures and instrumental accuracy estimates of TAO temperature, relative
833 humidity and radiation measurements.
- 834 Freitag, H. P. (1999), COARE seacat data : Calibrations and quality control procedures, Producer.
- 835 Freitag, H. P. (2001), Calibration procedures and instrumental accuracies for ATLAS wind measurements, Producer.



- 836 Froin, R., C. Gautier, & J. J. Morcrette (1988), Downward longwave irradiance at the ocean surface from satellite
837 data: Methodology and in situ validation, *J Geophys Res-Oceans*, 93(C1), 597-619,
838 <https://doi.org/10.1029/JC093iC01p00597>.
- 839 Fung, I. Y., D. E. Harrison, & A. A. Lacis (1984), On the variability of the net longwave radiation at the ocean
840 surface, *Rev Geophys*, 22(2), 177-193, <https://doi.org/10.1029/RG022i002p00177>.
- 841 Gelaro, R., W. McCarty, M. J. Suárez, R. Todling, A. Molod, L. Takacs, et al. (2017), The modern-era retrospective
842 analysis for research and applications, version 2 (MERRA-2), *J. Climate*, 30(14), 5419-5454,
843 <https://doi.org/10.1175/Jcli-D-16-0758.1>.
- 844 Grayek, S., J. Staneva, J. Schulz-Stellenfleth, W. Petersen, & E. V. Stanev (2011), Use of FerryBox surface
845 temperature and salinity measurements to improve model based state estimates for the German Bight, *J Marine Syst*,
846 88(1), 45-59, <https://doi.org/10.1016/j.jmarsys.2011.02.020>.
- 847 Gubler, S., S. Gruber, & R. S. Purves (2012), Uncertainties of parameterized surface downward clear-sky shortwave
848 and all-sky longwave radiation, *Atmos. Chem. Phys.*, 12(11), 5077-5098, <https://doi.org/10.5194/acp-12-5077-2012>.
- 849 Guo, Y., J. Cheng, & S. Liang (2019), Comprehensive assessment of parameterization methods for estimating clear-
850 sky surface downward longwave radiation, *Theoretical and Applied Climatology*, 135(3), 1045-1058,
851 <https://doi.org/10.1007/s00704-018-2423-7>.
- 852 Habets, F., J. Noilhan, C. Golaz, J. P. Goutorbe, P. Lacarrère, E. Leblois, et al. (1999), The ISBA surface scheme in
853 a macroscale hydrological model applied to the Hapex-Mobilhy area: Part I: Model and database, *Journal of*
854 *Hydrology*, 217(1), 75-96, [https://doi.org/10.1016/S0022-1694\(99\)00019-0](https://doi.org/10.1016/S0022-1694(99)00019-0).
- 855 Hack, J. J. (1998), Sensitivity of the simulated climate to a diagnostic formulation for cloud liquid water, *J. Climate*,
856 11(7), 1497-1515, [https://doi.org/10.1175/1520-0442\(1998\)011<1497:SOTSCT>2.0.CO;2](https://doi.org/10.1175/1520-0442(1998)011<1497:SOTSCT>2.0.CO;2).
- 857 Henderson - Sellers, B. (1984), A new formula for latent heat of vaporization of water as a function of temperature,
858 *Quart J Roy Meteor Soc*, 110(466), 1186-1190, <https://doi.org/10.1002/QJ.49711046626>.
- 859 Hersbach, H., B. Bell, P. Berrisford, S. Hirahara, A. Horányi, J. Muñoz - Sabater, et al. (2020), The ERA5 global
860 reanalysis, *Quart J Roy Meteor Soc*, 146(730), 1999-2049, <https://doi.org/10.1002/qj.3803>.
- 861 Hoffmann, L., G. Günther, D. Li, O. Stein, X. Wu, S. Griessbach, et al. (2019), From ERA-Interim to ERA5: the
862 considerable impact of ECMWF's next-generation reanalysis on Lagrangian transport simulations, *Atmos. Chem.*
863 *Phys.*, 19(5), 3097-3124, <https://doi.org/10.5194/acp-19-3097-2019>.
- 864 Idso, S. B., & R. D. Jackson (1969), Thermal radiation from the atmosphere, *J. Geophys. Res.*, 74(23), 5397-5403,
865 <https://doi.org/10.1029/JC074i023p05397>.
- 866 Iziomon, M. G., H. Mayer, & A. Matzarakis (2003), Downward atmospheric longwave irradiance under clear and
867 cloudy skies: Measurement and parameterization, *J Atmos Sol-Terr Phy*, 65(10), 1107-1116,
868 <https://doi.org/doi:10.1016/j.jastp.2003.07.007>.
- 869 Jiang, B., S. Liang, H. Ma, X. Zhang, Z. Xiao, X. Zhao, et al. (2016), GLASS daytime all-wave net radiation
870 product: Algorithm development and preliminary validation, *Remote Sens-Basel*, 8(3),
871 <https://doi.org/10.3390/rs8030222>.
- 872 Jiang, B., Y. Zhang, S. Liang, G. Wohlfahrt, A. Arain, A. Cescatti, et al. (2015), Empirical estimation of daytime net
873 radiation from shortwave radiation and ancillary information, *Agr Forest Meteor.*, 211-212, 23-36,
874 <https://doi.org/10.1016/j.agrformet.2015.05.003>.
- 875 Josey, S. A. (2003), A new formula for determining the atmospheric longwave flux at the ocean surface at mid-high
876 latitudes, *J Geophys Res-Oceans*, 108(C4), <https://doi.org/10.1029/2002jc001418>.
- 877 Josey, S. A., D. Oakley, & R. W. Pascal (1997), On estimating the atmospheric longwave flux at the ocean surface
878 from ship meteorological reports, *J Geophys Res-Oceans*, 102(C13), 27961-27972,
879 <https://doi.org/10.1029/97jc02420>.
- 880 Jost, G., R. Dan Moore, M. Weiler, D. R. Gluns, & Y. Alila (2009), Use of distributed snow measurements to test
881 and improve a snowmelt model for predicting the effect of forest clear-cutting, *Journal of Hydrology*, 376(1), 94-
882 106, <https://doi.org/10.1016/j.jhydrol.2009.07.017>.
- 883 Kjaersgaard, J. H., F. L. Plauborg, & S. Hansen (2007), Comparison of models for calculating daytime long-wave
884 irradiance using long term data set, *Agr Forest Meteor.*, 143(1-2), 49-63,
885 <https://doi.org/10.1016/j.agrformet.2006.11.007>.
- 886 Lake, B. J. (2003), Calibration procedures and instrumental accuracy estimates of ATLAS air temperature and
887 relative humidity measurements, NOAA Tech. Memo. OAR PMEL-123, 23.
- 888 Li, M., & C. F. M. Coimbra (2019), On the effective spectral emissivity of clear skies and the radiative cooling
889 potential of selectively designed materials, *Int J Heat Mass Tran*, 135, 1053-1062,
890 <https://doi.org/https://doi.org/10.1016/j.ijheatmasstransfer.2019.02.040>.



- 891 Li, M., Y. Jiang, & C. F. M. Coimbra (2017), On the determination of atmospheric longwave irradiance under all-
892 sky conditions, *Solar Energy*, 144, 40-48, <https://doi.org/10.1016/j.solener.2017.01.006>.
- 893 Lindau, R. (2012), *Climate atlas of the Atlantic Ocean: derived from the comprehensive ocean atmosphere data set*
894 (COADS), Springer Science & Business Media.
- 895 Lohmann, D., E. Raschke, B. Nijssen, & D. P. Lettenmaier (1998), Regional scale hydrology: II. Application of the
896 VIC-2L model to the Weser River, Germany, *Hydrological sciences journal*, 43(1), 143-158,
897 <https://doi.org/10.1080/02626669809492108>.
- 898 McPhaden, M. J., K. Ando, B. Bourles, H. P. Freitag, R. Lumpkin, Y. Masumoto, et al. (2010), The global tropical
899 moored buoy array, *Proceedings of OceanObs*, 9, 668-682.
- 900 McPhaden, M. J., A. J. Busalacchi, R. Cheney, J. R. Donguy, K. S. Gage, D. Halpern, et al. (1998), The Tropical
901 Ocean-Global Atmosphere observing system: A decade of progress, *J Geophys Res-Oceans*, 103(C7), 14169-14240,
902 <https://doi.org/10.1029/97JC02906>.
- 903 McPhaden, M. J., G. Meyers, K. Ando, Y. Masumoto, V. S. N. Murty, M. Ravichandran, et al. (2009), RAMA: the
904 research moored array for African-Asian-Australian monsoon analysis and prediction, *Bull. Amer. Meteor. Soc.*,
905 90(4), 459-480, <https://doi.org/10.1175/2008bams2608.1>.
- 906 Medovaya, M., D. E. Waliser, R. A. Weller, & M. J. McPhaden (2002), Assessing ocean buoy shortwave
907 observations using clear-sky model calculations, *J Geophys Res-Oceans*, 107,
908 <https://doi.org/10.1029/2000JC000558>.
- 909 Meyers, T. P., & R. F. Dale (1983), PREDICTING DAILY INSOLATION WITH HOURLY CLOUD HEIGHT
910 AND COVERAGE, *J Clim Appl Meteorol*, 22(4), 537-545, [https://doi.org/10.1175/1520-0450\(1983\)022<0537:pdihwc>2.0.co;2](https://doi.org/10.1175/1520-0450(1983)022<0537:pdihwc>2.0.co;2).
- 911 Mills, G. (1997), An urban canopy-layer climate model, *Theoretical and applied climatology*, 57(3), 229-244,
912 <https://doi.org/10.1007/BF00863615>.
- 913 Mousavi Maleki, S., H. Hizam, & C. Gomes (2017), Estimation of Hourly, Daily and Monthly Global Solar
914 Radiation on Inclined Surfaces: Models Re-Visited, *Energies*, 10(1), <https://doi.org/10.3390/en10010134>.
- 915 Moyer, K. A., & R. A. Weller (1997), Observations of surface forcing from the Subduction Experiment: A
916 comparison with global model products and climatological datasets, *J. Climate*, 10(11), 2725-2742,
917 [https://doi.org/10.1175/1520-0442\(1997\)010<2725:OOSFFT>2.0.CO;2](https://doi.org/10.1175/1520-0442(1997)010<2725:OOSFFT>2.0.CO;2).
- 918 Nandan, R., M. V. Ratnam, V. R. Kiran, & D. N. Naik (2022), Retrieval of cloud liquid water path using radiosonde
919 measurements: Comparison with MODIS and ERA5, *J Atmos Sol-Terr Phy*, 227,
920 <https://doi.org/10.1016/j.jastp.2021.105799>.
- 921 Nice, K. A., A. M. Coutts, & N. J. Tapper (2018), Development of the VTUF-3D v1.0 urban micro-climate model to
922 support assessment of urban vegetation influences on human thermal comfort, *Urban Climate*, 24, 1052-1076,
923 <https://doi.org/10.1016/j.uclim.2017.12.008>.
- 924 Ogunjobi, K. O., & Y. J. Kim (2004), Ultraviolet (0.280–0.400 μm) and broadband solar hourly radiation at
925 Kwangju, South Korea: analysis of their correlation with aerosol optical depth and clearness index, *Atmos Res*,
926 71(3), 193-214, <https://doi.org/10.1016/j.atmosres.2004.05.001>.
- 927 Oleson, K. W., G. B. Bonan, J. Feddema, M. Vertenstein, & C. S. B. Grimmond (2008), An Urban Parameterization
928 for a Global Climate Model. Part I: Formulation and Evaluation for Two Cities, *J. Appl. Meteor. Climatol.*, 47(4),
929 1038-1060, <https://doi.org/10.1175/2007JAMC1597.1>.
- 930 Pascal, R. W., & S. A. Josey (2000), Accurate Radiometric Measurement of the Atmospheric Longwave Flux at the
931 Sea Surface, *J. Atmos. Oceanic Technol.*, 17(9), 1271-1282, [https://doi.org/10.1175/1520-0426\(2000\)017<1271:ARMOTA>2.0.CO;2](https://doi.org/10.1175/1520-0426(2000)017<1271:ARMOTA>2.0.CO;2).
- 932 Paul, B. (2021), Retrospective on the resource for radiative cooling, *Journal of Photonics for Energy*, 11(4), 042106,
933 <https://doi.org/10.1117/1.JPE.11.042106>.
- 934 Pauwels, V. R. N., N. E. C. Verhoest, G. J. M. De Lannoy, V. Guissard, C. Lucau, & P. Defourny (2007),
935 Optimization of a coupled hydrology-crop growth model through the assimilation of observed soil moisture and leaf
936 area index values using an ensemble Kalman filter, *Water Resour Res*, 43(4),
937 <https://doi.org/10.1029/2006WR004942>.
- 938 Payne, R. E. (1972), Albedo of the sea surface, *J Atmos Sci*, 29(5), 959-970, [https://doi.org/10.1175/1520-0469\(1972\)029<0959:AOTSS>2.0.CO;2](https://doi.org/10.1175/1520-0469(1972)029<0959:AOTSS>2.0.CO;2).
- 939 Payne, R. E., & S. P. Anderson (1999), A new look at calibration and use of Eppley precision infrared radiometers.
940 Part II: Calibration and use of the Woods Hole Oceanographic Institution improved meteorology precision infrared
941 radiometer, *J. Atmos. Oceanic Technol.*, 16(6), 739-751, [https://doi.org/10.1175/1520-0426\(1999\)016<0739:ANLACA>2.0.CO;2](https://doi.org/10.1175/1520-0426(1999)016<0739:ANLACA>2.0.CO;2).



- 946 Pinardi, N., I. Allen, E. Demirov, P. De Mey, G. Korres, A. Lascaratos, et al. (2003), The Mediterranean ocean
947 forecasting system: first phase of implementation (1998–2001), *Annales Geophysicae*, 21(1), 3-20,
948 <https://doi.org/10.5194/angeo-21-3-2003>.
- 949 Pinker, R. T., A. Bentamy, K. B. Katsaros, Y. Ma, & C. Li (2014), Estimates of net heat fluxes over the Atlantic
950 Ocean, *J Geophys Res-Oceans*, 119(1), 410-427, <https://doi.org/10.1002/2013JC009386>.
- 951 Pinker, R. T., B. Zhang, R. A. Weller, & W. Chen (2018), Evaluating Surface Radiation Fluxes Observed From
952 Satellites in the Southeastern Pacific Ocean, *Geophys Res Lett*, 45(5), 2404-2412,
953 <https://doi.org/10.1002/2017gl076805>.
- 954 Prata, A. (1996), A new longwave formula for estimating downward clear - sky radiation at the surface, *Quart J Roy*
955 *Meteor Soc*, 122(533), 1127-1151, <https://doi.org/10.1002/qj.49712253306>Citations: 348.
- 956 Rigon, R., G. Bertoldi, & T. M. Over (2006), GEOTop: A distributed hydrological model with coupled water and
957 energy budgets, *Journal of Hydrometeorology*, 7(3), 371-388, <https://doi.org/10.1175/JHM497.1>.
- 958 Robinson, G. D. (1947), Notes on the measurement and estimation of atmospheric radiation, *Quart J Roy Meteor*
959 *Soc*, 73(315 - 316), 127-150, <https://doi.org/10.1002/qj.49707331510>.
- 960 Robinson, G. D. (1950), Notes on the measurement and estimation of atmospheric radiation–2, *Quart J Roy Meteor*
961 *Soc*, 76(327), 37-51, <https://doi.org/10.1002/qj.49707632705>.
- 962 Rossow, W. B., & Y. C. Zhang (1995), Calculation of surface and top of atmosphere radiative fluxes from physical
963 quantities based on ISCCP data sets: 2. Validation and first results, *J Geophys Res-Atmos*, 100(D1), 1167-1197,
964 <https://doi.org/10.1029/94JD02746>.
- 965 Rutan, D. A., S. Kato, D. R. Doelling, F. G. Rose, L. T. Nguyen, T. E. Caldwell, & N. G. Loeb (2015), CERES
966 synoptic product: Methodology and validation of surface radiant flux, *J. Atmos. Oceanic Technol.*, 32(6), 1121-
967 1143, <https://doi.org/10.1175/JTECH-D-14-00165.1>.
- 968 Saltelli, A., S. Tarantola, & K.-S. Chan (1999), A quantitative model-independent method for global sensitivity
969 analysis of model output, *Technometrics*, 41(1), 39-56, <https://doi.org/10.2307/1270993>
- 970 Satterlund, D. R. (1979), IMPROVED EQUATION FOR ESTIMATING LONG-WAVE-RADIATION FROM
971 THE ATMOSPHERE, *Water Resour Res*, 15(6), 1649-1650, <https://doi.org/10.1029/WR015i006p01649>.
- 972 Saucier, F. J., F. Roy, D. Gilbert, P. Pellerin, & H. Ritchie (2003), Modeling the formation and circulation processes
973 of water masses and sea ice in the Gulf of St. Lawrence, Canada, *J Geophys Res-Oceans*, 108(C8),
974 <https://doi.org/10.1029/2000JC000686>.
- 975 Schlosser, C. A., A. Robock, K. Y. Vinnikov, N. A. Speranskaya, & Y. Xue (1997), 18-Year Land-Surface
976 Hydrology Model Simulations for a Midlatitude Grassland Catchment in Valdai, Russia, *Mon. Wea. Rev.*, 125(12),
977 3279-3296, [https://doi.org/10.1175/1520-0493\(1997\)125<3279:YLSHMS>2.0.CO;2](https://doi.org/10.1175/1520-0493(1997)125<3279:YLSHMS>2.0.CO;2).
- 978 Schulz, E. W., S. A. Josey, & R. Verein (2012), First air-sea flux mooring measurements in the Southern Ocean,
979 *Geophys Res Lett*, 39(16), n/a-n/a, <https://doi.org/10.1029/2012gl052290>.
- 980 Schwarzschild, K. (1914), *Ueber Diffusion und Absorption in der Sonnenatmosphäre*. Sridhar, V., & R. L. Elliott
981 (2002), On the development of a simple downwelling longwave radiation scheme, *Agr Forest Meteor.*, 112(3), 237-
982 243, [https://doi.org/10.1016/S0168-1923\(02\)00129-6](https://doi.org/10.1016/S0168-1923(02)00129-6).
- 983 Staley, D. O., & G. M. Jurica (1972), Effective Atmospheric Emissivity under Clear Skies, *J Appl Meteorol*, 11(2),
984 349-356, [https://doi.org/10.1175/1520-0450\(1972\)011<0349:EAEUCS>2.0.CO;2](https://doi.org/10.1175/1520-0450(1972)011<0349:EAEUCS>2.0.CO;2).
- 985 Swinbank, W. C. (1963), Long - wave radiation from clear skies, *Quart J Roy Meteor Soc*, 89(381), 339-348,
986 <https://doi.org/10.1002/qj.49708938105>.
- 987 Thandlam, V., & H. Rahaman (2019), Evaluation of surface shortwave and longwave downwelling radiations over
988 the global tropical oceans, *SN Applied Sciences*, 1(10), <https://doi.org/10.1007/s42452-019-1172-2>.
- 989 Tiedtke, M. (1993), Representation of Clouds in Large-Scale Models, *Mon. Wea. Rev.*, 121(11), 3040-3061,
990 [https://doi.org/10.1175/1520-0493\(1993\)121<3040:ROCILS>2.0.CO;2](https://doi.org/10.1175/1520-0493(1993)121<3040:ROCILS>2.0.CO;2).
- 991 Vanhellemont, Q. (2020), Automated water surface temperature retrieval from Landsat 8/TIRS, *Remote Sens*
992 *Environ*, 237, <https://doi.org/10.1016/j.rse.2019.111518>.
- 993 Vertessy, R. A., T. J. Hatton, P. J. O'Shaughnessy, & M. D. A. Jayasuriya (1993), Predicting water yield from a
994 mountain ash forest catchment using a terrain analysis based catchment model, *Journal of Hydrology*, 150(2), 665-
995 700, [https://doi.org/10.1016/0022-1694\(93\)90131-R](https://doi.org/10.1016/0022-1694(93)90131-R).
- 996 Viúdez-Mora, A., M. Costa-Surós, J. Calbó, & J. A. González (2015), Modeling atmospheric longwave radiation at
997 the surface during overcast skies: The role of cloud base height, *J Geophys Res-Atmos*, 120(1), 199-214,
998 <https://doi.org/10.1002/2014jd022310>.



- 999 Wang, K., & S. Liang (2009a), Global atmospheric downward longwave radiation over land surface under all-sky
1000 conditions from 1973 to 2008, *J Geophys Res-Atmos*, 114(D19),
1001 <https://doi.org/https://doi.org/10.1029/2009JD011800>.
- 1002 Wang, T., J. Shi, Y. Ma, H. Letu, & X. Li (2020), All-sky longwave downward radiation from satellite
1003 measurements: General parameterizations based on LST, column water vapor and cloud top temperature, *ISPRS*
1004 *Journal of Photogrammetry and Remote Sensing*, 161, 52-60, <https://doi.org/10.1016/j.isprsjprs.2020.01.011>.
- 1005 Wang, W., & S. Liang (2009b), Estimation of high-spatial resolution clear-sky longwave downward and net
1006 radiation over land surfaces from MODIS data, *Remote Sens Environ*, 113(4), 745-754,
1007 <https://doi.org/10.1016/j.rse.2008.12.004>.
- 1008 Yang, F., & J. Cheng (2020), A framework for estimating cloudy sky surface downward longwave radiation from
1009 the derived active and passive cloud property parameters, *Remote Sens Environ*, 248,
1010 <https://doi.org/10.1016/j.rse.2020.111972>.
- 1011 Young, A. H., K. R. Knapp, A. Inamdar, W. Hankins, & W. B. Rossow (2018), The international satellite cloud
1012 climatology project H-Series climate data record product, *Earth System Science Data*, 10(1), 583-593,
1013 <https://doi.org/10.5194/essd-10-583-2018>.
- 1014 Yu, S., X. Xin, Q. Liu, H. Zhang, & L. Li (2018), Comparison of Cloudy-Sky Downward Longwave Radiation
1015 Algorithms Using Synthetic Data, Ground-Based Data, and Satellite Data, *J Geophys Res-Atmos*, 123(10), 5397-
1016 5415, <https://doi.org/10.1029/2017jd028234>.
- 1017 Zapadka, T., S. B. Woźniak, & B. Woźniak (2001), A simple formula for the net long-wave radiation flux in the
1018 Southern Baltic Sea, *Oceanologia*, 43(3), 265-277.
- 1019 Zhou, Y., & R. D. Cess (2001), Algorithm development strategies for retrieving the downwelling longwave flux at
1020 the Earth's surface, *J Geophys Res-Atmos*, 106(D12), 12477-12488, <https://doi.org/10.1029/2001jd900144>.
- 1021 Zhou, Y., D. P. Kratz, A. C. Wilber, S. K. Gupta, & R. D. Cess (2007), An improved algorithm for retrieving
1022 surface downwelling longwave radiation from satellite measurements, *J Geophys Res-Atmos*, 112(D15),
1023 <https://doi.org/10.1029/2006jd008159>.
- 1024